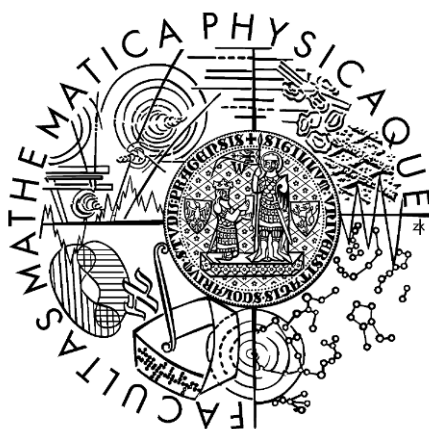


Charles University in Prague
Faculty of Mathematics and Physics

MASTER'S THESIS



Kateřina Kuřov

Light Emission from Materials Based on Silicon

Department of Thin Films, Institute of Physics, Academy of
Sciences of the Czech Republic

Supervisor: RNDr. Antonn Fejfar, CSc.

Study programme: Physics

Specialization: Optics and Optoelectronics

Acknowledgements

First of all, I would like to thank RNDr. Antonín Fejfar, CSc., my supervisor, for his guidance, his experience and ideas that formed this work.

I also want to express many thanks to RNDr. Petr Fojík, PhD. for teaching me to work with the STM microscope, his patience and his advices, and also for inestimable proof reading of this text.

My special thanks belong to prof. RNDr. Ivan Pelant, DrSc. for his excellent teaching and research experience which has invaluable contributed to this work. I am indebted to Mgr. Kateřina Dohnalová who prepared one series of samples. I am grateful to RNDr. Kateřina Luterová, PhD. for helping me with photoluminescence and electroluminescence measurements. I am also indebted to Ing. Emil Šípek, CSc. for the repair work and the adaptation made on the air STM microscope. Besides, I am grateful to the other members of the staff of the Department of Thin Films including RNDr. Jan Kočka, DrSc., Ing. Tomáš Mates, Mgr. Martin Ledinský, Petra Šnajdrová, and the others for technical assistance and friendly atmosphere.

Furthermore, I would like to thank Ing. Miroslav Buček from FSI VUT, Brno for providing his software SEA and adapting it for PE-STM measurements. I am also grateful to RNDr. Antonín Svoboda, CSc. from MFF UK, Prague for ray-tracing simulations of the detecting system and prof. Ing. Jaroslav Král, CSc. from FJFI ČVUT, Prague for performing the TRIM simulations of Si^+ ions in quartz.

Last but not least, I would like to express my thanks to my friends and my family who supported me during my university studies.

I hereby state that I have written this master's thesis by myself using only the cited references. I agree to lend it.

Prague, April 2004

Kateřina Kuřová

Contents

Abstract	3
Introduction	4
1 Semiconductors	7
1.1 Intrinsic Radiative Recombination	9
1.1.1 Direct Semiconductors	9
1.1.2 Indirect Semiconductors	9
1.2 Intrinsic Non-Radiative Recombination	10
1.3 Extrinsic Recombination	10
1.4 Quantum Efficiencies	11
1.5 Luminescence	12
1.6 Quantum Confinement	13
1.7 The Optical Constants of Semiconductors	14
1.8 Optical Constants in Inhomogeneous Materials	16
1.9 An Electromagnetic Wave at an Interface	17
1.10 The Interference in a Thin Layer	18
2 Light Emission in Silicon	21
2.1 Silicon in Photonics	22
2.1.1 Luminescence through Impurities	22
2.1.2 Quantum-Confined Structures	23
3 The Preparation of Samples	25
3.1 Ion Implantation	25
3.2 Electrochemical Etching	27
3.2.1 Porous Silicon	27
3.2.2 Isolation of Silicon Nanocrystals	28
3.2.3 Embedding in a Matrix	29

4	Results	31
4.1	Photoluminescence Measurements of the Samples Prepared by Spin-Coating	31
4.1.1	Experimental Setup	31
4.1.2	Photoluminescence Spectra	32
4.2	Electroluminescence Measurements of the Samples Prepared by Spin-Coating	33
4.2.1	Experimental Setup	33
4.2.2	Current-Voltage Curves and Integral Electroluminescence	34
4.2.3	Time Stability	37
4.2.4	Spectrally Integrated Electroluminescence with a Red Filter	39
4.3	Transmission Measurements of the Ion Implanted Samples . .	41
4.3.1	Results of the Transmission Measurements	41
4.3.2	The Model of the Optical Properties of the Nanocrystalline Layer	43
4.3.3	A Model of Interferences in a Thin Layer	44
4.3.4	A Model of Interference in Two Layers	46
4.4	Conductivity of the Ion Implanted Samples	50
4.5	Photon Emission Induced with an STM Tip	51
4.6	The Theoretical Background of Scanning Tunnelling Microscopy	52
4.6.1	STM Measurements	53
4.6.2	Photon Emission from Metals	55
4.6.3	Photon Emission from Semiconductors	55
4.6.4	Building the Experimental Setup for PE-STM	56
5	Discussion	61
5.1	Electrochemically Etched Silicon Nanocrystals	61
5.2	Ion Implanted Silicon Nanocrystals	62
5.3	The Experimental Setup for PE-STM	63
6	Conclusions	64
	Bibliography	68
	About the Author	69

Title: Light Emission from Materials Based on Silicon

Author: Kateřina Kůsová

Institute: Institute of Physics, Academy of Sciences of the Czech Republic

Supervisor: RNDr. Antonín Fejfar, CSc.

Supervisor's e-mail address: fejfar@fzu.cz

Abstract: New characterization techniques based on the use of local luminescence probes enable to study the properties of various nanostructures for optoelectronic applications with high (nanometric) spatial resolution. An experimental setup for measuring by one of these methods, namely, the photon emission induced with the tip of a scanning tunnelling microscope (PE-STM), has been built. In the future, this setup will be used for studying the luminescence from individual silicon nanocrystals in contrast to traditional macroscopic measurements providing only the information on the light emission from a large number of nanocrystals.

Nanocrystalline silicon is a promising material in which the light emission is enhanced, in contrast to monocrystalline silicon, by quantum confinement. Optoelectronic properties of two series of samples containing this interesting material were measured. Firstly, a weak electroluminescence signal and reasonable transport properties of samples prepared by embedding electrochemically etched silicon nanocrystals into SiO_2 matrix, and secondly, a conductive path created between individual silicon nanocrystals implanted in a silica glass slab were observed. Besides, for the latter series of samples, an interference model was developed and used to describe their structure. All these results are important for the future PE-STM measurements of these samples.

Keywords: nanocrystalline silicon, electroluminescence, photon emission induced with the tip of a scanning tunnelling microscope

Introduction

Ever since the first chip was designed, the trend towards faster and smaller computers has started. However, when the chips get smaller and smaller, there must be a limit, the least size of a functional component. Probably the most obvious problem that can possibly cause a malfunction of an electronic device is overheating [1]. In order to overcome these limitations, various ideas have been offered. These approaches include for example spintronics [2] based on the spin polarized current and using the the up- and down-state of an electron's spin to get the two basic units of information, or photonics [3], the replacement of electrons by photons. Concentrating on photonics, or optoelectronics—the combination of electronic circuits and photonic components, new light-emitting materials, preferably producible by the present-day technology, need to be developed. Therefore, as most present electronic devices are made from silicon, many laboratories nowadays aim their research into either the preparation of light-emitting silicon-based materials (or even a silicon laser) [1], [4], or the compatibility of the already used materials with silicon substrates [5].

As for the other consequence of the miniaturization trend, it is apparently the size of a structural detail that has to be studied. The sizes of optoelectronic and high-speed electronic components are under $1\text{ }\mu\text{m}$ even nowadays and are expected to be less than $0.1\text{ }\mu\text{m}$ in a few years. In certain cases (such as lasers or modulators for photonic applications) the active size of a device can even be in the order of nanometres [6]. Therefore, new methods of studying with high spatial resolution, characterizing not only the shape and the size of the studied structure, but also its optical (or electrical) properties, are essential.

Lately, several methods making possible the study of the optical properties with high spatial resolution has emerged largely due to the availability of sensitive light detectors. The most important advantage of these methods is the possibility to study the processes taking place in an individual nanometre-sized objects in contrast to the traditional measurements in which a macroscopic part of the studied sample is excited. This local excitation enables to overcome the inhomogeneous broadening of spectra resulting from the distribution in properties of the light-emitting centres, which can reveal new phenomena, such as the details on the structure of the spectra. Thus, the optical spectra of single molecules [7], semiconductor nanocrystals [8], [9] or various nanostructures [10], [11], [12] can be studied using such methods as microphotoluminescence (μ -PL) [13], cathodoluminescence (CL) [14], near-field scanning optical microscopy (NSOM) [15], or photon emission induced with the tip of a scanning tunnelling microscope (PE-STM, in literature often

called scanning tunnelling luminescence, or STL) [16].

It is very difficult to say which of these methods is the most convenient. μ -PL, the use of “traditional” photoluminescence together with a microscope, requires specially prepared samples with low concentration of individual light-emitting centres but is probably least demanding in special equipment. In both CL, based on collecting the photon emission excited by an electron beam (usually from an electron microscope), and NSOM, a scanning technique using near-field imaging, the resolution is limited reaching somewhat better values than 100 nm, in the former case due to the use of high-energy electron beam and in the latter case because of optical limits. A method that provides the highest resolution (several nanometres has been demonstrated [17]) but is, so far, probably not as widespread as the others, is PE-STM, using the tip of a scanning tunnelling microscope (STM) as the source of low-energy electrons of high intensity. The limitation of PE-STM measurements is given by its suitability only for samples that are conductive enough to allow tunnelling between the STM tip and the sample. On the other hand, transport properties of the studied samples can be measured by PE-STM, in contrast to the other methods.

The motivation of this work lies in building an experimental setup for measuring PE-STM in air. The work on this experiment in the Institute of Physics of the Academy of Sciences of the Czech Republic (FZÚ AVČR) was started by P. Fojtík [18] who successfully measured the photon emission from a testing material of polycrystalline silver using the STM placed in ultra high vacuum. However, the signal could only be obtained at low temperature and high tunnelling current, so a more sensitive detecting system was needed. Therefore he suggested a second experimental setup which I have built and tested using the STM in air. However, we encountered problems with signal intensity and a modelling approach had to be undertaken to optimize the photon collection.

Besides, my work lay in participating in the research on nanocrystalline silicon as a promising light emitting material since optical gain in silicon nanocrystals has been demonstrated [19]. In fact, the study of these materials was the reason for building the air-based PE-STM setup. The PE-STM measurement of silicon nanocrystals enables the excitation of single nanocrystals, allowing more thorough understanding of the processes responsible for the photon emission. The PE-STM study of silicon nanocrystals has not been, to our best knowledge, performed yet. However, the benefits of such a measurement can be illustrated by one of the measurements performed on porous silicon [20]. In this measurement, the PE-STM spectra obtained from exciting protrusions of various sizes were acquired. A blue shift in the photon emission peak with the decrease in the size of the protrusion was observed,

which confirms the importance of quantum confinement in the light emission from silicon nanostructures.

Concerning the nanocrystalline samples, I got acquainted with a unique sample preparation method used at FZÚ AVČR and then I measured the luminescence of the new series of samples with silicon nanocrystals that were especially prepared to enhance the electroluminescence signal from this type of structures. Moreover, I measured the transmission spectra of another samples containing silicon nanocrystals, namely, ion implanted samples. They are very interesting because they exhibit waveguiding effects [21]. In order to learn more about their structure I developed and used an interference model.

Chapter 1

Semiconductors

Semiconductors are crystalline (or amorphous) materials whose electrical conductivity lies between the conductivity of insulators and conductors. Furthermore, their conductivity can be influenced by changing the temperature, impurity density, or the intensity of incident light. Both some elements (in the IVth group in the periodical table) and various alloys (mostly obtained by combining either the elements in the IIIrd and the Vth group, or the elements in the IInd and the VIth group) are important semiconductor materials. The most important elements in semiconductor industry are depicted in Table 1.1.

II	III	IV	V	VI
Zinc	Aluminium	Silicon	Phosphorus	Sulphur
Cadmium	Gallium	Germanium	Arsenic	Selenium
Mercury	Indium	Tin	Antimony	Tellurium
	Thallium	Lead	Bismuth	Polonium

Table 1.1: *A part of the periodic table with semiconductor elements and elements used in semiconductor alloys **in bold**.*

The interesting properties of semiconductors are successfully used both in electronics and in photonics. Therefore, we can find them nearly everywhere around us—in computers, displays, printers, CD players, cellular phones, remote controls, washing-machines, etc.

The theoretical description of these materials is based on their band structure, i.e., the dependance of the energy of electron on their quasi-momentum $E(\vec{k})$. The quasi-momentum \vec{k} is in fact one of quantum numbers characterizing an electron in a crystal. It is suitable for describing an electron in a crystal because the quasi-momentum conservation law (deriving from the translational symmetry of the crystal lattice) applies.

The ideal (theoretical) band structure of a semiconductor comprises a conduction band and a valence band separated by a band-gap. We are usually interested in the shape $E(\vec{k})$ of the bands near the extremal values of the band-gap where they can be approximated with parabolas. In this one-electron approximation we consider an electron moving in an ideal crystal; the electron's mass is replaced with an effective value that represents the interaction with other electrons.

Under ideal circumstances at zero temperature all the electrons in the crystal would be in ground states in the valence band. In reality, however, the electrons are excited by various mechanisms into the conduction band. The process of electrons transferring from the valence band to the conductive one is responsible for the unique electrical properties of semiconductors. Their conduction band is, unlike in metals, empty under ideal conditions at zero temperature and their band-gap is, unlike in insulators, small enough to allow the excitation of an electron to the conduction band.

After the excitation an empty state (a hole) remains in the valence band. Naturally, the excited electron has a tendency to decrease its energy by recombining with a hole. The recombination can result in the emission of a photon, which is then called **radiative recombination** (or **luminescence** in semiconductors), or the energy can be transferred to other particles without emitting any light (**non-radiative recombination**).

Obviously, the recombination processes depend on the band structure. The semiconductors are divided into two groups according to their band structures: **direct semiconductors** in which the maximum of the valence band coincides to be directly under the minimum of the conduction band in the \vec{k} -space, and **indirect semiconductors** in which the maximum of the valence band and the minimum of the conduction band are located at different points of the \vec{k} -space.

Both optical and electrical properties of semiconductors can be changed by doping. The abundance of electrons arises from replacing some of the atoms in the crystal by atoms with excess valence electrons; these impurities are called **donors**. A material doped with atoms with less valence electrons can be prepared, too. These impurities are then referred to as **acceptors**. In the doped materials the impurities give rise to discrete energy levels within the band-gap. Thus, properties (and processes) connected with this discrete energy level are often referred to as **extrinsic** in contrast to **intrinsic** properties associated with the ideal band structure.

1.1 Intrinsic Radiative Recombination

1.1.1 Direct Semiconductors

In a direct semiconductor the process of radiative recombination is quite simple—the electron changes its position from the conduction band to the valence band where it recombines with a hole (Figure 1.1a, process I.). There are two important principles in the process: the principle of the conservation of energy and the principle of the conservation of \vec{k} -vector. As the energy of the electron-hole system decreases during the recombination, the difference between the initial and the final value of energy is carried away, in the case of radiative recombination, by a photon. On the other hand, the momentum of the photon is very low, so the electron's quasi-momentum does not change during the recombination and the transition is direct.

This radiative recombination process is quite efficient since it requires only the coincidence of an electron and a hole with the same quasi-momentum.

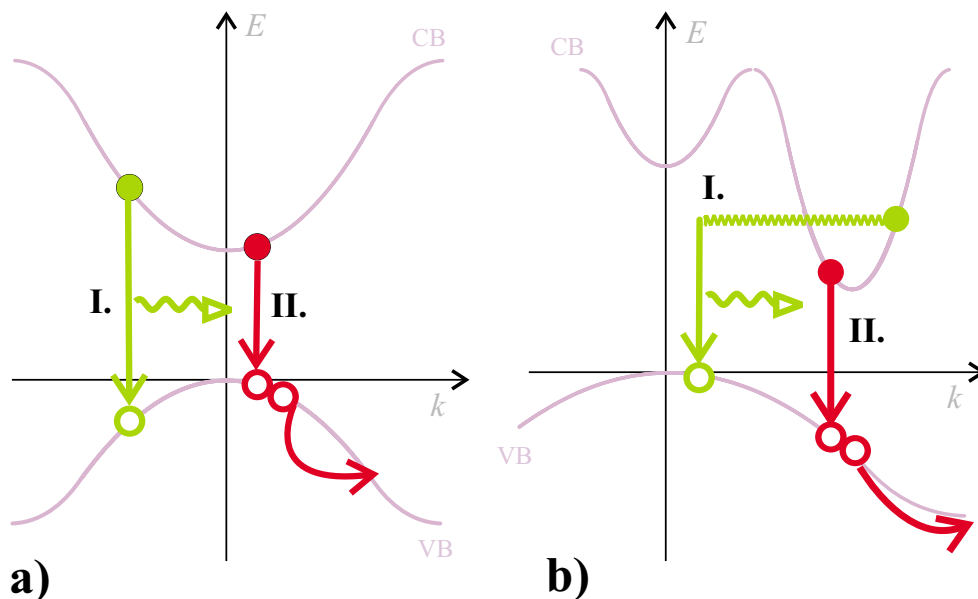


Figure 1.1: Examples of radiative (processes I.) and non-radiative (processes II.) recombination in a direct (a) and indirect (b) semiconductor.

1.1.2 Indirect Semiconductors

Obviously, the above described process of radiative recombination cannot happen in an indirect semiconductor. When an electron in the minimum of the conduction band (where most conducting electrons in the semiconductor

are present) changes its position to the maximum of the valence band (with the most probable presence of a hole), the value of the electron's quasi-momentum must vary, too. However, the photon's momentum is too low to compensate the difference, so another particle must participate in the process (Figure 1.1b, process I.). In the case of the radiative recombination in an indirect semiconductor the “participating particle” is a phonon whose energy is very low but whose quasi-momentum is high enough to supply the change in the quasi-momentum of the recombining electron.

The necessity of the presence of the third particle (a phonon) makes the radiative recombination in an indirect semiconductor much less (i.e., several orders of magnitude) probable (and, consequently, slower) than the radiative recombination in a direct semiconductor.

1.2 Intrinsic Non-Radiative Recombination

The difference of the energy before and after recombination can be transferred not only to a photon but also to another particle. We cannot observe any light emission as a result of such a process; in fact, the non-radiative recombination is a competing (and usually undesired) process to the radiative recombination.

The most common type of non-radiative recombination is **Auger recombination**. Auger recombination is generally a process in which the difference in energy is transferred to another electron in the conduction band (or a hole in the valence band, as is depicted in Figures 1.1a, 1.1b, processes II). This recombination process takes place in both the direct and indirect semiconductor, often with the probability of the same order of magnitude (see Table 1.2).

	GaAs	Si
τ_r	1 ns	500 μ s
τ_A	10 μ s	3 μ s

Table 1.2: *The comparison of the radiative and non-radiative intrinsic processes in direct semiconductors, such as GaAs, and indirect semiconductors, such as Si. The processes are characterized by the lifetime of an electron before it recombines radiatively (τ_r) or by the Auger process (τ_A). After [22].*

1.3 Extrinsic Recombination

In reality, discrete energy levels can be found in the band-gap. These levels arise from various lattice defects, such as impurities, dislocations, or grain

boundaries and can act either as **recombination centres** (in case they are able to capture both electrons and holes) or **traps** (if the probability of capturing one type of carriers is higher). The recombination via recombination centres in the band-gap can be both radiative and non-radiative.

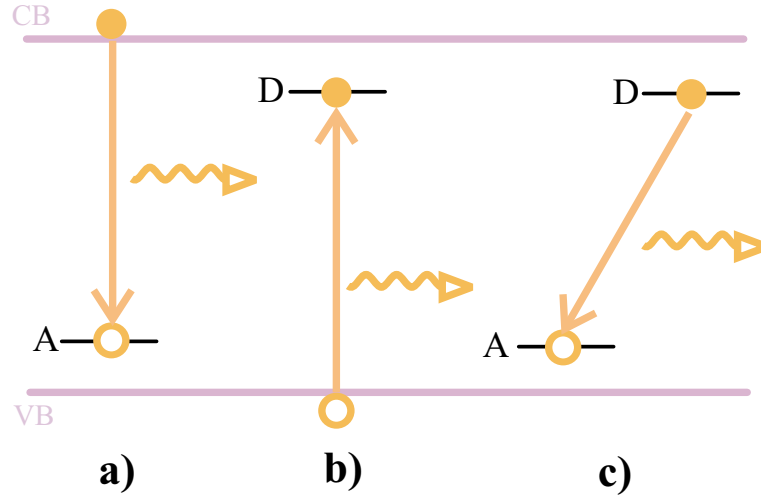


Figure 1.2: *Three most important mechanisms of the recombination via discrete energy levels in the band-gap.*

The following mechanisms of the recombination via discrete energy levels in the band-gap are the most important:

The band-impurity recombination: a free electron (or hole) in the conduction (valence) band recombines with a hole (electron) bound on an acceptor (donor) energy level (see Figure 1.2a and 1.2b, respectively).

The recombination of donor-acceptor pairs: an electron bound on a donor energy level recombines with a hole bound on an acceptor energy level (Figure 1.2c).

The recombination via isoelectric impurities: important mostly in indirect semiconductors because it can enhance radiative recombination. The strong localization of an electron at the impurity gives rise to an uncertainty in the value of its quasi-momentum which allows a quasi-direct recombination without the assistance of a phonon.

1.4 Quantum Efficiencies

In order to distinguish between different efficiencies of the light generation in various materials the **internal quantum efficiency** of radiative recom-

bination η_i has been introduced. It can be defined as the ratio of the radiative recombination rate (\mathcal{R}_r) and the total recombination rate (\mathcal{R}) (that are indirectly proportional to the corresponding radiative and non-radiative lifetimes τ_r and τ_{nr} , respectively)

$$\eta_i = \frac{\mathcal{R}_r}{\mathcal{R}} = \frac{\frac{1}{\tau_r}}{\frac{1}{\tau}} = \frac{\tau_{nr}}{\tau_r + \tau_{nr}}. \quad (1.1)$$

The internal quantum efficiency quantitatively compares the probabilities of radiative and non-radiative recombination. In direct semiconductors, the internal quantum efficiency is high (~ 1), but in indirect semiconductors the competitive non-radiative processes have shorter lifetimes than the radiative ones, which leads to low internal quantum efficiency of radiative recombination, or, in other words, the indirect semiconductors are inefficient light emitters.

Besides, the **external quantum efficiency** is used, too.

1.5 Luminescence

The photon emission, arising from some of the above described mechanisms, can, obviously, be experimentally observed and is called **luminescence**. It can be defined as *the light emitted by matter which exceeds the Planck's radiation law and whose lifetime is greater than 10^{-10} s* (which excludes the reflected or scattered light). Thus, luminescence is the emitted light that is not caused by solely the rise of temperature.

Various kinds of luminescence depend on the injection mechanisms:

Photoluminescence: the light emission that results from the excitation of electrons into the conduction band by photons. The energy of a photon absorbed in a material is transformed into the excitation energy of an electron. Photoluminescent materials are used for layers in fluorescent lights, or, if lifetime is sufficiently long, for the at-night-luminous hands of clocks and watches.

Electroluminescence: the carriers are injected electrically. Light-emitting diodes (LED) and semiconductor lasers are based on electroluminescence.

Chemiluminescence: the energy comes from an exothermic chemical reaction. It is used e.g. in the diver's glowing sticks that start to shine when they are "broken" (two different materials mix in the stick which is followed by a chemical reaction exciting the chemiluminescence).

Cathodoluminescence: the luminescence arises from the incidence of electrons with high energy. We can come across this phenomenon in our televisions as the picture we see is created by an electron beam.

Bioluminescence: the light is produced by a chemical reaction which originates in an organism. The best-known case of bioluminescence is that of fireflies but most luminous organisms are found in seas, ranging from one-cell algae and bacteria to deep-sea fishes.

Sonoluminescence: the luminescence produced by ultrasonic devices has been discovered, too.

1.6 Quantum Confinement

The properties of volume semiconductors result from their periodic structure. However, with reducing the size of a semiconductor under the order of micrometers in one or more dimensions its physical properties, such as the band structure, the density of states, and optical and electrical properties, start to change. This change is due to the **quantum confinement effect**, the confinement of the motion of carriers. The quasi-two-dimensional structure, with the confinement in one dimension, is called a *quantum well*, in case of a quasi-one-dimensional structure we talk about a *quantum wire*, and the quasi-zero-dimensional structure is called a *quantum dot* (or a *nanocrystal*, which usually refers to the samples, not the ideal structure).

The basic description of the optical properties of a quantum dot is based on solving the Schrödinger equation for an electron-hole pair in infinite spherical confinement potential. Three regimes can be distinguished, comparing the radius of the quantum dot R with the Bohr radius of an exciton a_B in the given material:

$$a_B = 4\pi\epsilon_0 \frac{\hbar^2 \epsilon_r}{e^2 m_r}. \quad (1.2)$$

In Equation (1.2) ϵ_0 is the permittivity of vacuum, \hbar is the reduced Planck's constant, ϵ_r is the relative permittivity of the material, e is the charge of an electron, and m_r is the reduced mass of the electron-hole pair given by

$$\frac{1}{m_r} = \frac{1}{m_e} + \frac{1}{m_h}. \quad (1.3)$$

The three regimes are as follows:

Strong coupling: $R \ll a_B$, the Coulombic interaction of the electron-hole pair is small with respect to the confinement potential. The electron and the hole behave as free particles. There is an increase in the value

of the lowest optical transition E_g^{QDsc} (corresponding to the band-gap E_g^{bulk})

$$E_g^{QDsc} = E_g^{bulk} + \frac{\hbar^2}{2m_r} \left(\frac{\pi}{R} \right)^2. \quad (1.4)$$

Weak coupling: $R \gg a_B$, the Coulombic interaction is dominant and the motion of the electron-hole pair is quantized. The band-gap value E_g^{QDwc} is then

$$E_g^{QDwc} = E_g^{bulk} + \frac{\hbar^2}{2(m_e + m_h)} \left(\frac{\pi}{R} \right)^2. \quad (1.5)$$

Intermediate coupling: the theoretical description is difficult. The difference in the effective masses of an electron and a hole ($m_e < m_h$) can be used; the motion of the electron is then quantized and the hole interacts with the electron by Coulombic interaction.

1.7 The Optical Constants of Semiconductors

Till now, the properties of semiconductors has been described mostly from the microscopic point of view. However, the macroscopic insight can also be useful.

The propagation of an electromagnetic wave is described by **Maxwell equations**

$$\begin{aligned} \nabla \times \vec{\mathcal{E}} + \frac{\partial \vec{B}}{\partial t} &= 0 & \nabla \cdot \vec{\mathcal{D}} &= \rho \\ \nabla \times \vec{\mathcal{H}} - \frac{\partial \vec{D}}{\partial t} &= \vec{j} & \nabla \cdot \vec{\mathcal{B}} &= 0 \end{aligned} \quad (1.6)$$

The behaviour of a wave in a material is usually described with the vector of electric induction $\vec{\mathcal{D}}$ and magnetic induction $\vec{\mathcal{B}}$ (assuming that the material is linear, isotropic, and without free charges ($\rho = 0$))

$$\vec{\mathcal{D}}(\vec{r}, t) = \epsilon \vec{\mathcal{E}}(\vec{r}, t) = \epsilon_0 \epsilon_r \vec{\mathcal{E}}(\vec{r}, t) \quad (1.7)$$

and

$$\vec{\mathcal{B}}(\vec{r}, t) = \mu \vec{\mathcal{H}}(\vec{r}, t) = \mu_0 \mu_r \vec{\mathcal{H}}(\vec{r}, t) \quad (1.8)$$

respectively. In these formulas $\vec{\mathcal{E}}$ ($\vec{\mathcal{H}}$) is the intensity of electric (magnetic) field, and ϵ_0 (μ_0) is the permittivity (permeability) of free space. Nevertheless, the properties of a material are often described with the **permittivity** ϵ (or a dimensionless unit of relative permittivity ϵ_r). The value of relative permeability μ_r is one for paramagnetic and diamagnetic materials. Finally, \vec{j} stands for the current density and ρ for the charge density.

Assuming a harmonic planar wave ($\vec{\mathcal{A}}$ stands for any of vectors $\vec{\mathcal{E}}$, $\vec{\mathcal{D}}$, $\vec{\mathcal{H}}$, or $\vec{\mathcal{B}}$, $\vec{q} = \frac{\omega}{c} \vec{s}$ for the wave vector, ω is the circular frequency, c the velocity of light in the given material and \vec{s} is a unit vector describing the orientation of the vector \vec{q})

$$\vec{\mathcal{A}} = \vec{\mathcal{A}}_0 \exp[i(\vec{q} \cdot \vec{r} - \omega t)] = \vec{\mathcal{A}}_0 \exp[i(q\vec{s} \cdot \vec{r} - \omega t)], \quad (1.9)$$

and linear isotropic non-magnetic material without free charges, the Maxwell equations can be written as

$$\begin{aligned} \vec{s} \times \vec{E} &= -c\mu_0 \vec{\mathcal{H}} & \vec{s} \cdot \vec{E} &= 0 \\ \vec{s} \times \vec{H} &= c\left(\varepsilon - i\frac{\sigma}{\omega}\right) \vec{\mathcal{E}} & \vec{s} \cdot \vec{H} &= 0 \end{aligned} \quad (1.10)$$

where the conductivity σ is given by

$$\vec{j} = \sigma \vec{\mathcal{E}} \quad (1.11)$$

If a wave travels through a medium with an interface, the condition for the continuity of the electric and magnetic induction vectors (i.e., their tangential components must remain unchanged when travelling through the interface) can simply be derived from these equations.

Except for the relative permittivity, a material can also be described by the **refractive index** n characterizing the velocity of light in the material c compared to the velocity of light in vacuum c_0

$$c = \frac{c_0}{n}, \quad n > 1 \quad (1.12)$$

The relationship between the refractive index and relative permittivity can be expressed as

$$n^2 = \varepsilon_r \mu_r \quad (1.13)$$

These material constants are often defined as complex numbers $\hat{\varepsilon}$ and \hat{n} , with the real parts ε_1 and n , and imaginary parts ε_2 and κ , respectively

$$\hat{\varepsilon} = \varepsilon_1 - i\varepsilon_2 = \hat{n}^2 = (n - i\kappa)^2. \quad (1.14)$$

If we consider an electric wave (1.9), it will travel through a material as

$$\vec{\mathcal{E}} = \vec{\mathcal{E}}_0 \exp[i(q\hat{n}\vec{r} \cdot \vec{s} - \omega t)] = \vec{\mathcal{E}}_0 \exp\left[i\left(\frac{\omega n}{c_0} \vec{r} \cdot \vec{s} - \omega t\right)\right] \exp\left[-\frac{\omega \kappa}{c_0} \vec{r} \cdot \vec{s}\right]. \quad (1.15)$$

The complex refractive index \hat{n} (and permittivity) then comprises both the normal refractive index n and the absorption coefficient α

$$\frac{\alpha}{2} = \frac{\omega \kappa}{c_0}. \quad (1.16)$$

The complex refractive index is used to describe absorbing materials because the absorption can be simply included into the refractive index and formulas for absorbing and non-absorbing materials are analogous.

1.8 Optical Constants in Inhomogeneous Materials

The optical properties of an inhomogeneous material can be characterized by effective optical constants if the wavelength of the incident wave is much greater than the average size of inhomogeneities. Then the wave cannot distinguish between individual scattering centres and an effective value of the optical constants characterizes the inhomogeneous material from the macroscopic point of view.

In the **theory of effective medium** the typical microstructure of the inhomogeneous material is replaced by a random cell embedded in the effective medium. Supposing that the inhomogeneous material is both translationally and rotationally symmetric, the random cell is spherical. The relative permittivity characterizing the effective medium is then defined by the condition that the electromagnetic waves in the proximity of the random cell and in the effective medium cannot be distinguished.

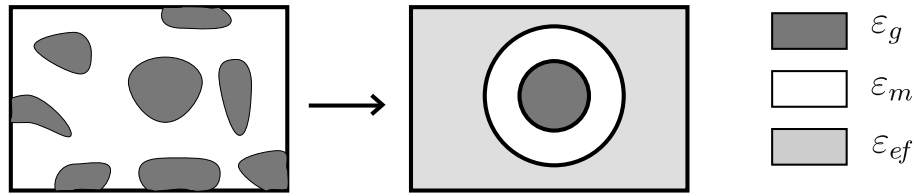


Figure 1.3: *The replacement of an inhomogeneous material consisting of grains and a matrix with an effective medium and a random cell.*

Obviously, the effective permittivity of the inhomogeneous medium depends on the permittivities of the materials of which the inhomogeneous material is composed. In the case of small grains (with permittivity ε_g) embedded in a matrix (with permittivity ε_m) the random cell representing this microstructure is a sphere with the core of the grain material surrounded by the layer of the matrix material (see Figure 1.3.)

The change in the electric field caused by a two-layer sphere such as the random cell can be estimated; the effective permittivity is then determined by requiring this change to be zero. Thus, a formula for the effective permittivity ε_{ef} can be deduced. In the case of grains embedded in a matrix the so-called **Maxwell-Garnett formula** [23] for effective permittivity is as follows

$$\frac{\varepsilon_{ef} - \varepsilon_m}{\varepsilon_{ef} + 2\varepsilon_m} = f \frac{\varepsilon_g - \varepsilon_m}{\varepsilon_g + 2\varepsilon_m}. \quad (1.17)$$

The fill factor f is the volume ratio of grains to the whole layer

$$f = \frac{V_{\text{grains}}}{V_{\text{grains}} + V_{\text{matrix}}}. \quad (1.18)$$

1.9 An Electromagnetic Wave at an Interface

If we consider a wave (1.9) at the interface of two materials with refractive indexes n_1, n_2 (the situation is schematically shown in Figure 1.4), the wave splits into a reflected $\vec{\mathcal{E}}_r$ and transmitted $\vec{\mathcal{E}}_t$ one:

$$\begin{aligned} \vec{\mathcal{E}}_r &= r(\omega) \vec{\mathcal{E}} \\ \vec{\mathcal{E}}_t &= t(\omega) \vec{\mathcal{E}} \end{aligned} \quad (1.19)$$

where the amplitude coefficients of reflection and transmission are denoted r and t , respectively. We can see from the requirement of the equality of the phases at the interface that the frequency ω of the wave is unchanged and both the reflected and transmitted waves stays at the same plane as the incident wave.

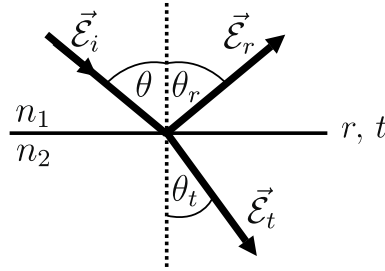


Figure 1.4: The reflection and transmission at a planar interface.

The angle of reflection θ_r remains the same as the angle of incidence θ whereas the angle of refraction θ_r is determined by the **Snell's law**

$$n_1 \sin \theta = n_2 \sin \theta_t. \quad (1.20)$$

The amplitude coefficients of reflection r and transmission t for $\vec{\mathcal{E}}$ perpendicular (\perp) or parallel (\parallel) to the plane of incidence can then be calculated from the **Fresnel equations** (deduced from the requirement of the continuity of the wave at an interface)

$$\begin{aligned} r_{\perp} &= \frac{\mathcal{E}_r^{\perp}}{\mathcal{E}_i^{\perp}} = -\frac{\sin(\theta - \theta_t)}{\sin(\theta + \theta_t)} = \frac{n_1 \cos \theta - n_2 \cos \theta_t}{n_1 \cos \theta + n_2 \cos \theta_t} \\ r_{\parallel} &= \frac{\mathcal{E}_r^{\parallel}}{\mathcal{E}_i^{\parallel}} = \frac{\tan(\theta - \theta_t)}{\tan(\theta + \theta_t)} = \frac{n_2 \cos \theta - n_1 \cos \theta_t}{n_2 \cos \theta + n_1 \cos \theta_t} \\ t_{\perp} &= \frac{\mathcal{E}_t^{\perp}}{\mathcal{E}_i^{\perp}} = \frac{2 \cos \theta \sin \theta_t}{\sin(\theta + \theta_t)} = \frac{2 n_1 \cos \theta}{n_1 \cos \theta + n_2 \cos \theta_t} \\ t_{\parallel} &= \frac{\mathcal{E}_t^{\parallel}}{\mathcal{E}_i^{\parallel}} = \frac{2 \cos \theta \sin \theta_t}{\sin(\theta + \theta_t) \cos(\theta - \theta_t)} = \frac{2 n_1 \cos \theta}{n_2 \cos \theta + n_1 \cos \theta_t} \end{aligned} \quad (1.21)$$

which can be simplified for the special case of a perpendicularly incident wave ($\theta = \theta_t = \frac{\pi}{2}$)

$$r_{\perp/\parallel} = \frac{n_1 - n_2}{n_1 + n_2} \quad t_{\perp/\parallel} = \frac{2n_1}{n_1 + n_2}. \quad (1.22)$$

In these formulas either real or complex refractive indexes can be used.

The coefficients of reflection and transmission for intensities (the reflectance R and the transmittance T) can then be written as

$$\begin{aligned} I_r(\omega) &= \vec{\mathcal{E}}_r(\omega) \cdot \vec{\mathcal{E}}_r^*(\omega) = |r(\omega)\vec{\mathcal{E}}|^2 = R(\omega)|\vec{\mathcal{E}}|^2 = R(\omega)I \\ I_t(\omega) &= \vec{\mathcal{E}}_t(\omega) \cdot \vec{\mathcal{E}}_t^*(\omega) = |t(\omega)\vec{\mathcal{E}}|^2 = T(\omega)|\vec{\mathcal{E}}|^2 = T(\omega)I \end{aligned} \quad (1.23)$$

1.10 The Interference in a Thin Layer

An electromagnetic wave incident at an interface is partly reflected and partly transmitted as was described above. The partial reflection and transmission of the wave in a thin layer (i.e., its thickness is less than the coherence length of the light) results into a series of transmitted and reflected waves with phase difference. The waves can then interfere.

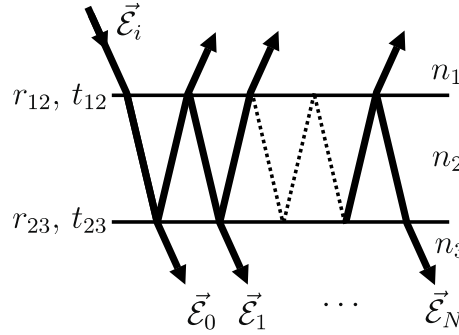


Figure 1.5: *Interference in a thin layer.*

If we want to describe the interference, we can consider an electromagnetic wave $\vec{\mathcal{E}}_i$ transmitting and reflecting at planar interfaces between three media with refractive indexes n_1 , n_2 , and n_3 . The corresponding coefficients of transmission and reflection (calculated from the Fresnel equations (1.21)) are then denoted r_{12} , t_{12} , etc., depending on the subscript of the refractive index and the direction in which the wave propagates (see Figure 1.5). The transmitted, twice reflected, etc., N -times reflected wave in the middle layer can then be expressed as

$$\begin{aligned} \vec{\mathcal{E}}_0 &= t_{12}t_{23}\vec{\mathcal{E}}_i \exp(i\delta) \\ \vec{\mathcal{E}}_1 &= t_{12}r_{23}r_{21}t_{23}\vec{\mathcal{E}}_i \exp(3i\delta) \\ &\vdots \\ \vec{\mathcal{E}}_N &= t_{12}(r_{23}r_{21})^N t_{23}\vec{\mathcal{E}}_i \exp[(2N+1)i\delta]. \end{aligned} \quad (1.24)$$

The phase difference is denoted δ and equals

$$\delta = \frac{2\pi}{\lambda} n_2 d \quad (1.25)$$

(d is the thickness of the layer). The resulting transmitted wave $\vec{\mathcal{E}}_T$ is then the sum of the individual transmitted waves

$$\vec{\mathcal{E}}_T = t_{12}t_{23} \exp(i\delta) \sum_{N=0}^M (r_{21}r_{23})^N \exp(2N\delta) \vec{\mathcal{E}}_i \approx \frac{t_{12}t_{23} \exp(i\delta)}{1 + r_{12}r_{23} \exp(2i\delta)} \vec{\mathcal{E}}_i. \quad (1.26)$$

Thus, the complex transmittance of the whole system can be defined

$$T_{\text{layer}} = \frac{\text{Re}(n_3)}{\text{Re}(n_1)} \left| \frac{t_{12}t_{23} \exp(i\delta)}{1 + r_{12}r_{23} \exp(2i\delta)} \right|^2. \quad (1.27)$$

The only material parameters that need to be known if we want to estimate the transmission from Equation (1.27), are the refractive indexes n_1 , n_2 , and n_3 , because the coefficients of transmission and reflection can be evaluated from Fresnel equations (1.21). The absorption can be included into the imaginary parts of the refractive indexes.

Abelés matrix method [24] is usually used for more complicated systems than one thin layer. It is based on solving the Maxwell equations (1.10) with the requirement of the continuity of tangential components of the $\vec{\mathcal{E}}$ and $\vec{\mathcal{H}}$ vectors [25], similarly as when deriving the Fresnel equations. In the case of a medium consisting of several homogeneous layers, the electric and magnetic fields (x_0 in subscript denotes the x -component “above” the interface, x in subscript stands for the x -component “under” the interface, and similarly) can be connected by means of a **characteristic matrix** [25]

$$\begin{pmatrix} \mathcal{E}_x(z) \\ \mathcal{H}_y(z) \end{pmatrix} = \begin{pmatrix} \cos \varphi & \frac{i}{Y} \sin \varphi \\ iY \sin \varphi & \cos \varphi \end{pmatrix} \begin{pmatrix} \mathcal{E}_{x0}(z) \\ \mathcal{H}_{y0}(z) \end{pmatrix} \quad (1.28)$$

where

$$\varphi(z) = q_0(z - z_0) \sqrt{n^2 - n_0^2 \sin^2 \theta_0} = q(z - z_0). \quad (1.29)$$

In Equation (1.29) q describes the wave vector of the wave propagating in the medium with refractive index n if the preceding layer has the refractive index n_0 and the angle of refraction θ_0 , from the plane z_0 to the plane z . The formula for Y differs for the vector $\vec{\mathcal{E}}$ polarized perpendicularly (\perp) or parallel (\parallel) to the plane of incidence; it can be written as

$$Y_{\perp} = \sqrt{\frac{\varepsilon_0}{\mu_0} (n^2 - n_0^2 \sin^2 \theta_0)} \quad \text{and} \quad Y_{\parallel} = -\sqrt{\frac{\varepsilon_0}{\mu_0} \frac{n^2}{n^2 - n_0^2 \sin^2 \theta_0}}, \quad (1.30)$$

respectively.

The main advantage of this approach lies in the fact that the characteristic matrix of a medium comprising more layers can be obtained simply by multiplying the matrices of the individual layers in the right order. It can even be generalized for a medium with continuously changing properties (refractive index) by considering a wave propagating through a system of infinitesimally thin layers.

Chapter 2

Light Emission in Silicon

A great deal of recent electronic circuits are based on silicon (its most important physical properties are introduced in Table 2.1). The reasons for the

Energy gap	1.12 eV
Crystal structure	cubic diamond
Lattice constant	5.43 Å
Density	2328 kg m ⁻³
Melting point	1410 °C
Conductivity	$3 \times 10^{-4} \Omega^{-1}\text{cm}^{-1}$

Table 2.1: *The most important physical properties of bulk silicon. All the values excluding the melting point correspond to the room temperature. After [26].*

widespread use of silicon in electronics are numerous:

- Its **energy gap** of 1.12 eV is ideal for room temperature operation.
- It can be **easily passivated** by oxidation. During this process, an insulating layer of SiO₂ appears.
- As a semiconductor consisting of only **one element** it is well suitable for the production of monocrystals. In semiconductors comprising more than one element more parameters must be kept constant during the preparation, which makes the production of a one-element monocrystal less difficult than the production of a more-elements one.
- It is **chemically stable** and **non-toxic**.
- It is **available**. It is the second most abundant element in the Earth's crust, of which it makes up 27.7 % by weight, as is depicted in Table 2.2.

It is found largely as silicon oxides such as sand (silica), quartz, or rock crystal, then in amethyst, agate, flint, jasper and opal.

Oxygen	46.6 %	Calcium	3.6 %
Silicon	27.7 %	Sodium	2.8 %
Aluminum	8.1 %	Potassium	2.6 %
Iron	5.0 %	Magnesium	2.1 %

Table 2.2: *The most abundant elements in the Earth’s crust (by weight). After [27].*

As it has started to be used in industry on account of the qualities mentioned above, it has also become **cheap** (due to mass production) and **easy to handle** since a lot of experience has been gained.

2.1 Silicon in Photonics

Photonics is one of possible ways of solving the current problems of electronics (or, said in a better way, the problems which will limit the development of electronics in the future)—*overheating* and *information delay* [1].

Photons have numerous advantages over electrons, including the facts, that they do not dissipate heat, are immune to cross-talks, have low transmission losses and less information delay. Therefore, the photonic chips built into the electronic circuits can improve the performance of the used devices.

Photonics has boomed recently. Photonics-based devices include such widespread appliances as liquid crystal displays (LCD), compact discs (CD), or laser printers. Furthermore, silicon microphotonic devices have been demonstrated [1], e.g., silicon-based optical waveguides with low losses, tuneable optical filters, fast switches (\sim ns) and optical modulators (\sim GHz).

However, when combining the advantages of silicon and photonics, we will encounter one big problem because bulk silicon is a very poor light emitter due to its indirect band-gap as was described in the previous Chapter. Nevertheless, various approaches have been undertaken to overcome this disadvantage. The most important ones are **luminescence through impurities** and **quantum-confined structures**.

2.1.1 Luminescence through Impurities

The approach of doping silicon with **isoelectric impurities** has been undertaken. Even though it works with other semiconductors (probably best-known is indirect-gap GaP [28] since effective LED’s at room temperature

can be made from it), it fails with silicon [4]. The intensity of the light emission from silicon doped with isoelectric impurities at room temperature is low.

Another, and more successful, way of making a light-emitting material from silicon is **the doping with the rare-earth elements**, e.g., with erbium [4]. When silicon is doped with the ions of Er^{3+} and then irradiated, a transition in the $4f$ -shell in the electron cloud of erbium atoms ($^1\text{I}_{3/2} \rightarrow ^1\text{I}_{5/2}$) takes place (with certain probability). The deexcitation occurs through numerous competing processes, including the radiative deexcitation. The interesting thing about the radiated photon is its wavelength of $1.54 \mu\text{m}$ that can be important in optical telecommunications.

The rare-earth-doped silicon has become a very promising light-emitting material. Not only photoluminescence, but also electroluminescence from this material has been observed. Metal-oxide-semiconductor (MOS) structure with erbium-doped SiO_2 showed the external quantum efficiency of 10 % [29]. Moreover, an idea of an optical amplifier is based on the erbium doped SiO_2 waveguides [30]. As the erbium ions do not absorb the excitation light well, the waveguides are doped with silicon nanocrystals, too. They absorb light well and transfer the energy to the amplifying erbium ions. Thus, the silicon nanocrystals serve as an “antenna” for the erbium ions [30].

2.1.2 Quantum-Confined Structures

The discovery of effective luminescence from porous silicon in the visible range at room temperature [31] initiated the interest in silicon nanostructures. Porous silicon is prepared by electrochemical etching of a silicon wafer by hydrofluoric acid. As the acid attacks the surface of silicon, its structure changes into a combination of quantum wires and quantum dots. The reasons of the enhanced photoluminescence, quoted here with regards to silicon nanocrystals because they are the material that will be studied in this diploma thesis, are as follows:

- **The quantum confinement** (in a strong-coupling region) causes partial change from the indirect transition in bulk crystals to a quasi-direct one in nanocrystals as is schematically depicted in Figure 2.1. The wave function in a nanocrystal is localized in \vec{x} -space. Because of the Heisenberg’s uncertainty principle it must be delocalized in \vec{p} -space and thus in k -space. This delocalization makes the quasi-direct transition possible, which increases the radiative recombination rates.
- On the other hand, the nanocrystal occupies only a **small volume** that is usually almost **without defects**. Moreover, its **surface is**

passivated because the nanocrystal is imbedded in a matrix. These two phenomena lead to a decrease in the non-radiative recombination rates.

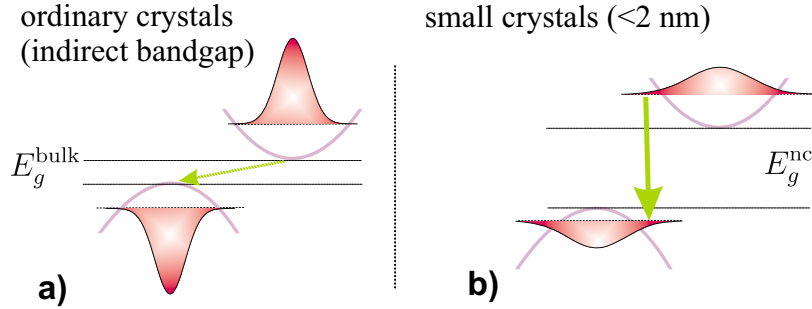


Figure 2.1: The change from an indirect transition (a) in bulk crystals to a quasi-direct one (b) in small Si nanocrystals.

Moreover, the energy gap increases with decreasing size of a nanocrystal (Section 1.6). This phenomenon leads to a blue shift of the luminescence. As (very weak) luminescence from bulk silicon (at low temperature) is situated in the infrared range corresponding to its energy gap of 1.12 eV, the luminescence from silicon nanocrystals is shifted to visible range.

Another promising property of silicon nanocrystals is the **decrease in free-carrier-absorption**. This phenomenon stems again from the larger energy gap in nanocrystals and the consequent situation of luminescence at lower wavelengths. As the free-carrier-absorption decreases with decreasing wavelength ($\alpha_{FCA} \sim \lambda^2$), the photoluminescence is less reabsorbed in nanocrystals. Materials with high free-carrier-absorption cannot be used as an active material for lasers, because the free-carrier absorption prevents inversion. The decrease in the free-carrier-absorption in silicon nanocrystals would make a future construction of a silicon laser possible.

Chapter 3

The Preparation of Samples

In my diploma thesis I will focus on silicon nanocrystals (nc-Si) as a silicon-based light-emitting material. Although there are numerous methods of the preparation of nc-Si, such as the plasma enhanced chemical vapour deposition [32], laser ablation [33], sputtering [34], or organic synthesis [35], I will concentrate only on ion implantation and electrochemical etching. Samples being to my disposal were prepared by these two methods.

3.1 Ion Implantation

Ion implantation is a wide-spread method with a variety of possible applications, ranging from modifying surface mechanical properties (such as friction, adhesion, or corrosion) and optical properties (index changes for an anti-reflection coating or wavelength-selective mirrors) to semiconductor doping. All materials, metals as well as insulators and semiconductors, can be used as a substrate for implantation. It is even possible to introduce buried layers (such as nc-Si layers) with completely different properties from the substrate if the implantation dose is high enough.

As for the preparation of a nc-Si layer in a silica glass slab, a layer with an excess concentration of Si^+ ions in silica glass is introduced by means of an Si^+ ion beam. The depth of the Si^+ ions layer within the silica glass can be changed by varying the energy of the ion beam because the energy of ions decide their range in the substrate. The usual value of energy is in the order of 100 keV.

After the implantation the whole sample is annealed to the temperature of about 1000–1100 °C. During the annealing, the Si^+ ions merge into single silicon nanocrystals with the diameter in order of nanometres. The density of these nanocrystals can again be controlled; samples with higher doses (i.e., with higher numbers of Si^+ ions per a unit of surface of the sample in the ion

beam) during the implantation result in samples with higher concentrations of nc-Si in the layer.

The concentration of nanocrystals is not constant throughout the layer but depends on the depth: it decreases at the top and bottom edges of the layer whereas it is higher in the middle part (see Figure 3.1).

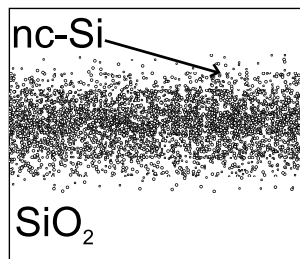


Figure 3.1: *A cross-section of a sample prepared by ion implantation.*

The depth layer profiles of ion implanted layers generally range from Gaussian peaks to asymmetrical peaks with one part tailing towards the direction from which the ions were implanted [36].

Despite the high cost of the equipment essential for the ion implantation it is an important and commonly used technique for preparing nc-Si because both the dose and the depth within the substrate can be controlled. Furthermore, the surface of the sample is of high optical quality.

Description of samples	
Sample	Dose [cm^{-2}]
II03	3×10^{17}
II04	4×10^{17}
II05	5×10^{17}
II06	6×10^{17}
Preparation parameters	
substrate	1 mm thick silica glass slab (Infrasil)
energy of Si^+ beam	400 keV
implantation temperature	room temperature
annealing	1 hour in N_2 at 1100 °C
	1 hour in 5 % H_2 in N_2 at 500 °C

Table 3.1: *The parameters used in ion implantation.*

The samples studied in this diploma thesis were prepared in the Research School of Physical Sciences and Engineering at the Australian National University in Canberra, Australia. The preparation parameters are listed in Table 3.1. The preparation resulted in the nanocrystalline layer within a glass slab with the mean diameter of nanocrystals between 4–5 nm.

One of these samples, namely, the sample with $4 \times 10^{17} \text{ cm}^{-2}$ dose was adapted for the measurement of transport properties. Two thin parts with the shape of a rectangular prism were cut off from the sample, the faces were polished and the two parts were pasted together so that the nanocrystalline layers were situated next to each other (as is depicted in Figure 3.2). This procedure was suggested by J. Valenta. The structure was contacted (top indium-tin-oxide (ITO) contact and bottom silver glue). This sample will be referred to as II04P.

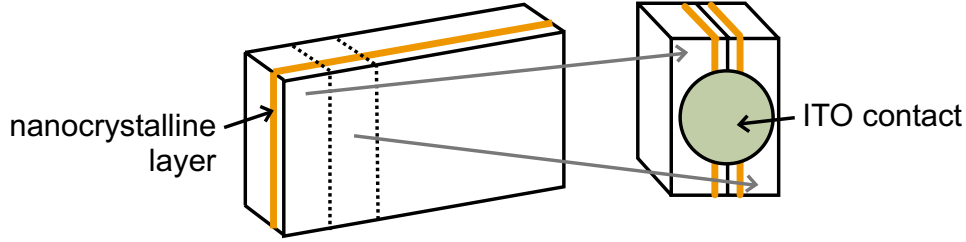


Figure 3.2: *The adaption of ion-implanted samples for the measurement of transport properties. Two part were cut off and then pasted together.*

3.2 Electrochemical Etching

The method of preparing nc-Si used in our laboratory in the Institute of Physics of the Academy of Sciences of the Czech Republic (FZÚ AVČR) was suggested by V. Švrček [37] and developed by K. Dohnalová [38]. The preparation is based on electrochemical etching, providing porous silicon (por-Si), and comprises three steps: firstly, the process of electrochemical etching, secondly, the isolation of nanocrystals, and finally embedding nanocrystals in a matrix. This method is relatively cheap and easy compared to e.g. ion implantation. It enables the preparation of samples with varying concentration of nanocrystals, and, moreover, it provides samples whose photoluminescence is blue-shifted compared to samples prepared by ion implantation, which can be seen if the photoluminescence spectra of the electrochemically etched nanocrystals measured in this master's thesis (Figure 4.2) and the photoluminescence spectra of the ion implanted samples [21] are compared. The blue shift is important for the search for optical gain. On the other hand, it results, for the time being, in quite inhomogeneous samples [38].

3.2.1 Porous Silicon

The setup used for standard electrochemical etching of a monocrystalline silicon wafer by hydrofluoric acid consists of a bottom rust-free contact (an

anode) on which the etched silicon wafer is placed, then of an etching teflon chamber and a platinum cathode as is depicted in Figure 3.3. The platinum cathode rotates during the etching process to make the resulting por-Si more homogeneous.

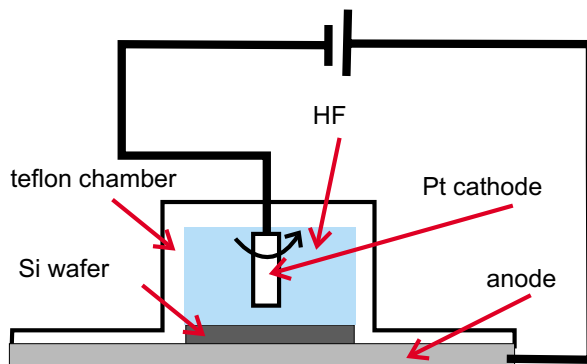


Figure 3.3: A scheme of the setup used for electrochemical etching of a silicon wafer.

The properties of prepared por-Si strongly depend on the used set of parameters; etching parameters utilized in our laboratory are summarized in Table 3.2.

dilution of 50 % HF and UV ethanol	1:3
etching time	2 hours
etching current density	1.6 mA/cm ²
illumination	natural room light
type of the Si wafer	P
surface structure of the Si wafer	polished
temperature	room temperature

Table 3.2: The used set of etching parameters.

The prepared por-Si exhibits orange photoluminescence when illuminated by ultraviolet lamp in air at room temperature (see Figure 3.4).

3.2.2 Isolation of Silicon Nanocrystals

The isolation of nc-Si takes place by means of mechanical pulverization resulting in a powder material consisting of single nanocrystals with the diameter of about 3 nm and nanocrystalline clusters [38]. The pulverization of por-Si surface of about 10 cm² yields 0.1 mg of nc-Si.



Figure 3.4: *The photoluminescence of porous silicon can be observed with a naked eye. After [38].*

In order to get rid of the biggest (and consequently least luminescent) nanocrystals, they are dispersed in UV ethanol. The biggest ones are separated by sedimentation and the ethanol with nc-Si is filtered through a filter with $1\text{ }\mu\text{m}$ holes.

However, on account of a large active surface the photoluminescence of both por-Si and nc-Si is not stable and decays with time. Therefore the surface must be passivated; in our case, nc-Si are embedded in a matrix.

3.2.3 Embedding in a Matrix

A unique sol-gel-based technique has been developed in the laboratory of FZÚ AVČR. Pulverized nc-Si are embedded in SiO_2 matrix arising from the solidification of a commercially available dilution. The so-called spin-on-diffusant P509 (P509), produced by an American company FILMTRONICS that is standardly used in silicon-based technology for doping silicon wafers with phosphorus, serves as a substrate material. After a few hours in air the dilution solidifies at room temperature into a transparent SiO_2 layer.

In order to embed the nc-Si in the SiO_2 matrix the nanocrystals are added to P509 and the mixture is treated in an ultrasonic bath to achieve more homogeneous samples. The mixture can solidify either in a spectroscopic cuvette, resulting in samples for optical measurements, or on an Si substrate.

After embedding in the matrix, nanocrystals still exhibit orange photoluminescence that can be observed by a naked eye at room temperature under ultraviolet excitation. In contrast to por-Si, the photoluminescence of embedded nc-Si is relatively stable on longer time scale [38].

Regarding possible optoelectronic application, electrical excitation needs to be used instead of optical one. Therefore, conductive samples are essential. Thus, thin-film samples of nc-Si in SiO_2 on silicon substrate were prepared. The preparation of the samples took place in collaboration with the Institute of Anorganic Chemistry AVČR in Řež by a spin-coating method with

parameters summarized in Table 3.3.

Description of samples	
ncSi02	reference (blank) sample on N-type Si wafer
ncSi03	N-type Si wafer with nanocrystalline layer
ncSi05	P-type Si wafer with nanocrystalline layer
Preparation parameters	
nc-Si to P509 ratio	6 mg : 0.1 ml
rotation rate	500 rot/s
rotation time	30 s
acceleration	100 rot/s ²

Table 3.3: *The parameters for spin-coating.*

As for the contacts, ITO circles 2 mm in diameter were sputtered at room temperature on the top side of the samples and the sample was attached to an aluminium foil using a conductive silver glue. The resulting structure is shown in Figure 3.5 (the (nc-Si+SiO₂)-layer is about 300 nm thick).

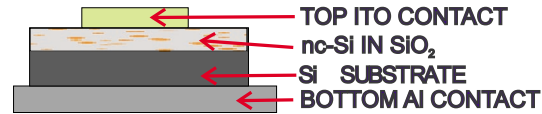


Figure 3.5: *A cross-section of the sample prepared by spin-coating method.*

Chapter 4

Results

This master's thesis was focused on the measurement of the optoelectronic properties of nanocrystalline-silicon samples and on building an experimental setup for PE-STM, with the future outlooks for measuring the optoelectronic properties of nanocrystalline silicon with high spatial resolution. In the following Sections the measurements performed on the samples presented in the previous Chapter are introduced. The last Section of this Chapter deals with building the setup for PE-STM.

4.1 Photoluminescence Measurements of the Samples Prepared by Spin-Coating

A photoluminescence measurement provides us with the information on the most important optical properties of the studied material. Therefore, it is the basic optical characterization method revealing (spectrally resolved) light emission of the material. In case of various nanostructures the preliminary information on their size can be derived from them assuming the quantum confinement model.

4.1.1 Experimental Setup

All the photoluminescence measurement were performed at FZÚ AVČR. The experimental setup for measuring photoluminescence is shown in Figure 4.1. The sample is excited with a continuous wave He-Cd laser at 435 nm (or 325 nm), then the photoluminescence signal is collected by a glass fiber, and transferred to a *H20* monochromator. The photoluminescence spectrum is finally detected with an *Andor* CCD camera. The measurable wavelengths range from 391 to 1079 nm with the step of 0.174 nm. In these measurements,

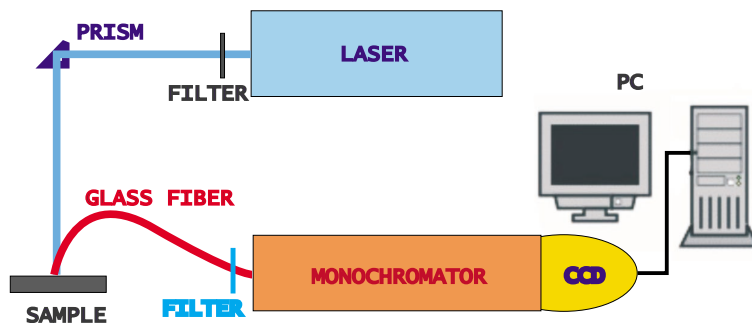


Figure 4.1: *The experimental setup used for photoluminescence measurements.*

the monochromator slit of $100\ \mu\text{m}$ was used and the CCD camera was cooled to $-50\ ^\circ\text{C}$ to suppress the dark noise.

4.1.2 Photoluminescence Spectra

The photoluminescence of the samples prepared by spin-coating (Table 3.3) was measured. The measured spectra can be seen in Figure 4.2. All the measurements were performed at room temperature. The maximum of the

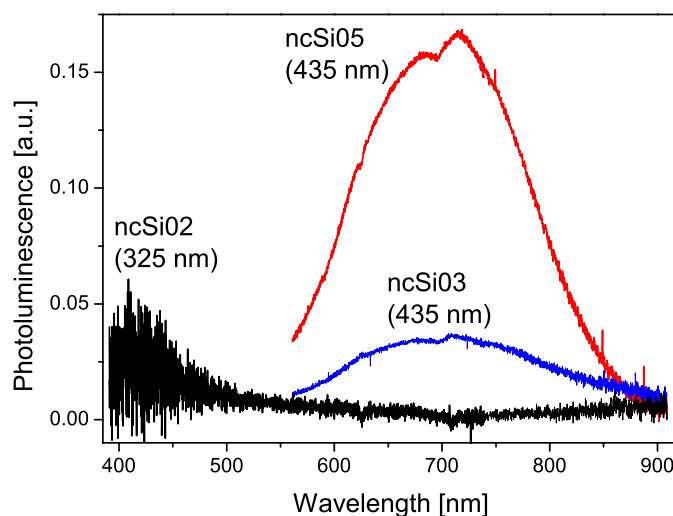


Figure 4.2: *The measured photoluminescence spectra of the ncSi samples. The excitation wavelength is shown in brackets. The notch at 695 nm is an artifact of the measurement.*

spectra with nanocrystals (at about 720 nm) is attributed to the photolu-

minescence of nc-Si (the position of the maximum corresponds to the diameter of the nanocrystal of about 3 nm). The band is quite broad; its width (FWHM \sim 200 nm) is caused by wide distribution of sizes of individual nanocrystals. The shape of the band is very similar to that of the samples prepared previously by the same technique [38]. The intensity of photoluminescence of the sample ncSi03 was lower than that of ncSi05 despite the same concentration of nc-Si in P509 during the preparation. The difference can be partially caused by not exactly the same adjustment of the positions of the sample and the glass fiber during the measurement.

The reference sample (pure P509) exhibits no photoluminescence in the region between 600 and 800 nm in which the nc-Si photoluminescence is situated when excited with 435 nm line. Nevertheless, a weak blue photoluminescence was observed under the excitation with the 325 nm line. This blue photoluminescence from the reference sample is probably caused by the defects in SiO₂.

4.2 Electroluminescence Measurements of the Samples Prepared by Spin-Coating

Practically, optoelectronic devices are not excited optically but electrically. However, in order to get an electroluminescence (EL) signal from a material apart from a photoluminescence one, good transport properties are necessary, which is not easy to achieve in a nanocrystalline material. Thus, not only optical but also electrical properties need to be studied.

4.2.1 Experimental Setup

In order to describe the optoelectronic properties current-voltage (I - V) curves along with spectrally integrated EL were studied in FZÚ AVČR using an experimental setup shown in Figure 4.3. Required voltage (current) is applied to the sample and then the flowing current (or resulting voltage) is measured (both with a source/electrometre *Keithley 237*) to obtain the I - V curves. The EL signal from the sample placed in the chamber is collected with a glass waveguide, then detected with a photomultiplier tube (*R636-10*). Photon counter *Hamamatsu C5410* is used to integrate the EL signal (the integration time is 1 s). The whole experiment is automated and controlled by a personal computer (PC).

EL spectra can also be measured in this setup simply by adding a monochromator with a chopper and a lock-in amplifier. However, the measured EL was too weak to enable to obtain any measurable signal after passing through the monochromator-chopper system.

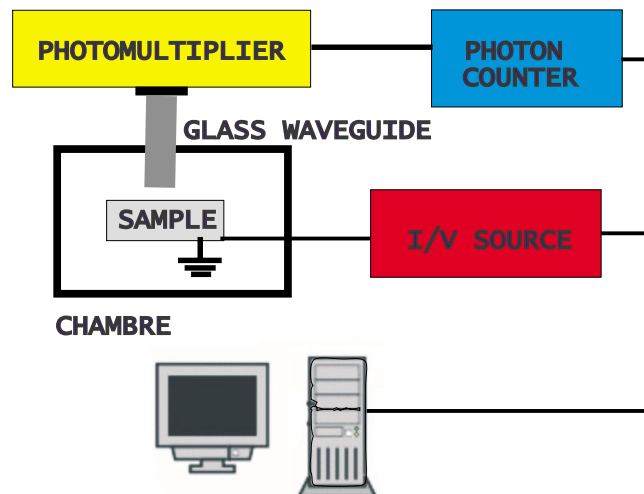


Figure 4.3: *The experimental setup used for electroluminescence measurements.*

4.2.2 Current-Voltage Curves and Integral Electroluminescence

The I - V curves and EL-voltage curves of the samples prepared by spin-coating (Table 3.3) were measured. These samples were prepared to achieve better optoelectronic properties and thus higher EL signal with high concentration of nanocrystals in the SiO_2 layer (6 mg of nc-Si powder in 0.1 ml of P509 corresponds to about $180 \times 10^{16} \text{ nc/cm}^3$ compared to $45 \times 10^{16} \text{ nc/cm}^3$ as a maximum in previously prepared samples [38]).

The top ITO contacts of the samples were biased whereas the bottom Al contacts were grounded. Thus, the polarity quoted hereafter corresponds to the polarity applied to the $(\text{SiO}_2 + \text{nc-Si})$ -layer. As a doped substrate is used, the negative bias applied to the SiO_2 layer on N-type Si (and the resulting positive bias applied to the Si wafer) can be regarded as a reverse bias (samples ncSi02 and ncSi03) whereas the negative bias applied to the SiO_2 layer on P-type Si can be viewed as a forward bias.

The results are displayed in Figures 4.4–4.6. The measured curves were reproducible when measuring different samples though the measured EL signal usually slightly decreased during the several first measurements after which it became stable.

The voltage range in which individual samples were measured, depended on their electrical properties. When the bias applied to a sample was increased above a critical value (“a breakdown voltage”) a sudden change in the I - V curve appeared—the current decreased radically (to nA) and the EL signal disappeared. There were usually regions preceding the breakdown in

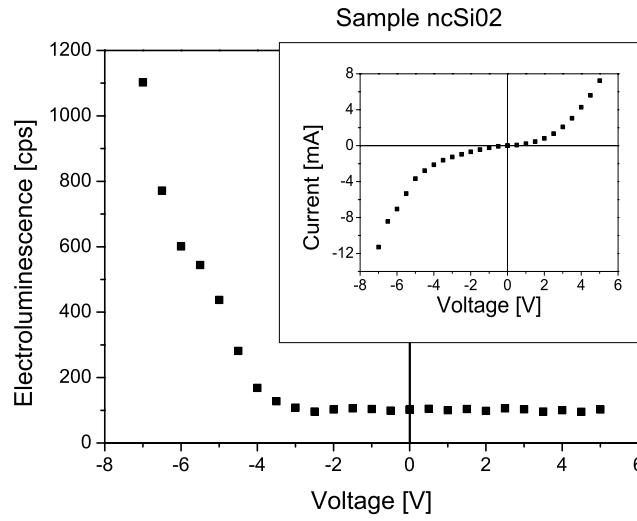


Figure 4.4: The electroluminescence signal and current-voltage curve of the reference sample ncSi02. The polarity of the bias corresponds to the polarity applied to the SiO_2 layer.

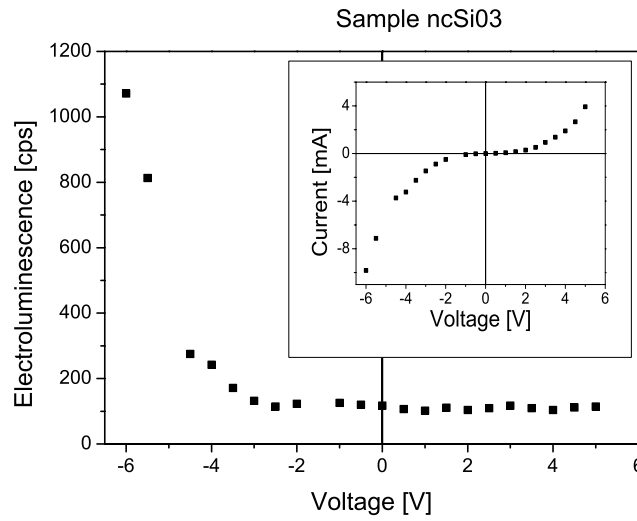


Figure 4.5: The electroluminescence signal and current-voltage curve of the sample ncSi03. The polarity of the bias corresponds to the polarity applied to the $(\text{SiO}_2 + \text{nc-Si})$ layer. The source compliance (Keithley 237) was set to 10 mA.

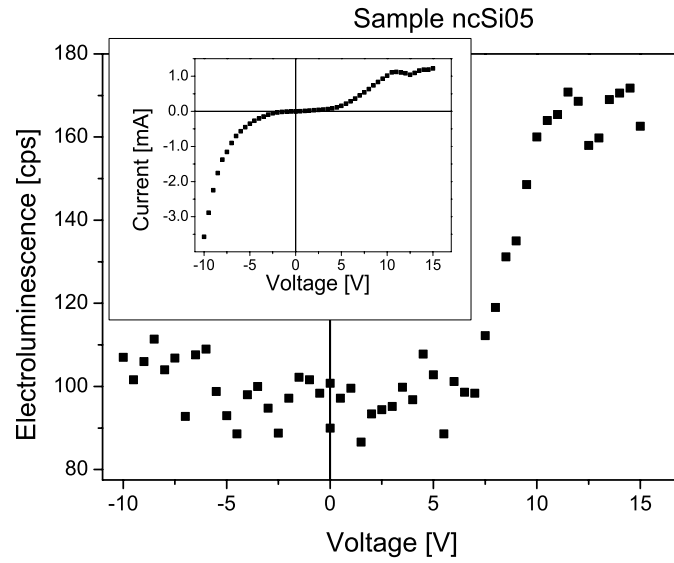


Figure 4.6: The electroluminescence signal and current-voltage curve of the sample ncSi05. The polarity of the bias corresponds to the polarity applied to the ($\text{SiO}_2 + \text{nc-Si}$) layer.

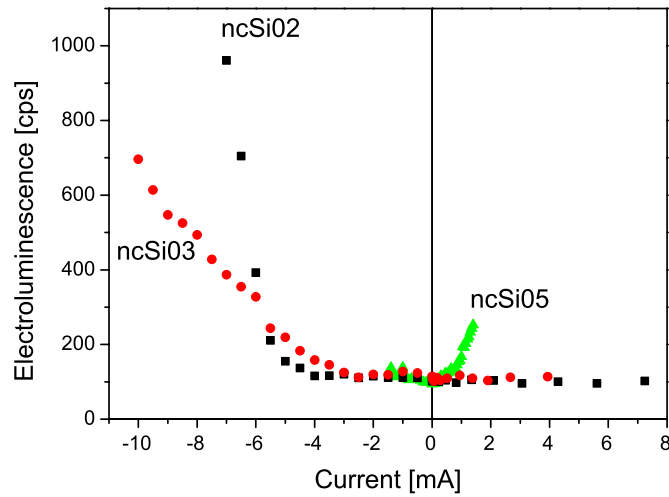


Figure 4.7: The electroluminescence as a function of current of the measured samples. The polarity of the bias corresponds to the polarity applied to the SiO_2 layer.

which the current remained more or less constant, which was accompanied by the decrease in the EL signal (as can be seen in Figure 4.6). The value of the breakdown voltage was about 10 V for samples ncSi02 and ncSi03 (though it was slightly lower for the sample ncSi02) and between 15 and 20 V for the sample ncSi05.

The conductivity of the measured samples was estimated to be in the order of $10^{-7} \Omega^{-1}\text{cm}^{-1}$ (this value can be compared to the conductivity of monocrystalline silicon which is $3 \times 10^{-4} \Omega^{-1}\text{cm}^{-1}$) with very similar values for the samples ncSi02 and ncSi03 and somewhat lower value for the sample ncSi05.

A weak EL signal from both the nanocrystalline samples was observed when reversely biased. However, contrary to expectations, EL signal from the reference sample ncSi02 with no nanocrystals and no photoluminescence except for a weak photoluminescence band in the blue region was observed (again in the reverse bias).

This behaviour was confirmed by the measurement of EL as a function of current that can be seen in Figure 4.7. This plot is in fact also a comparison of the EL signal of the samples prepared by spin-coating.

4.2.3 Time Stability

In order to see if the EL signal is stable on a longer time scale the time stability measurements were performed using the same experimental setup as in the previous case (Figure 4.3). A constant current was forced to flow through the sample and both the intensity of EL and the resulting voltage were measured. The resulting plots are shown in Figure 4.8.

The intensity of EL was found to be stable over the interval of several minutes except for a slight decrease in the EL signal at the beginning that can be seen in the inset of Figure 4.8a.

Two types of behaviour were observed in general, occurring according to the value of the voltage. If the voltage resulting from the flowing current was sufficiently low, both the EL signal and the voltage were stable as is displayed in Figure 4.8a. However, if the voltage exceeded a critical value, the increase in the voltage (decrease in the conductivity) of the sample was observed (as in Figure 4.8b), which usually led to the disappearance of the EL signal after several minutes. However, after contacting the sample in a slightly different spot in the same contact the electrical properties got better again approaching the same values as before the measurement (though a decrease in the EL intensity occurred).

The stability of the EL signal over the interval of several minutes could allow us to measure an EL spectrum that would reveal more details on the origin of the measured EL. Some attempts of measuring EL spectra were performed. However, the signal was still too low, probably as a result of broad spectra.

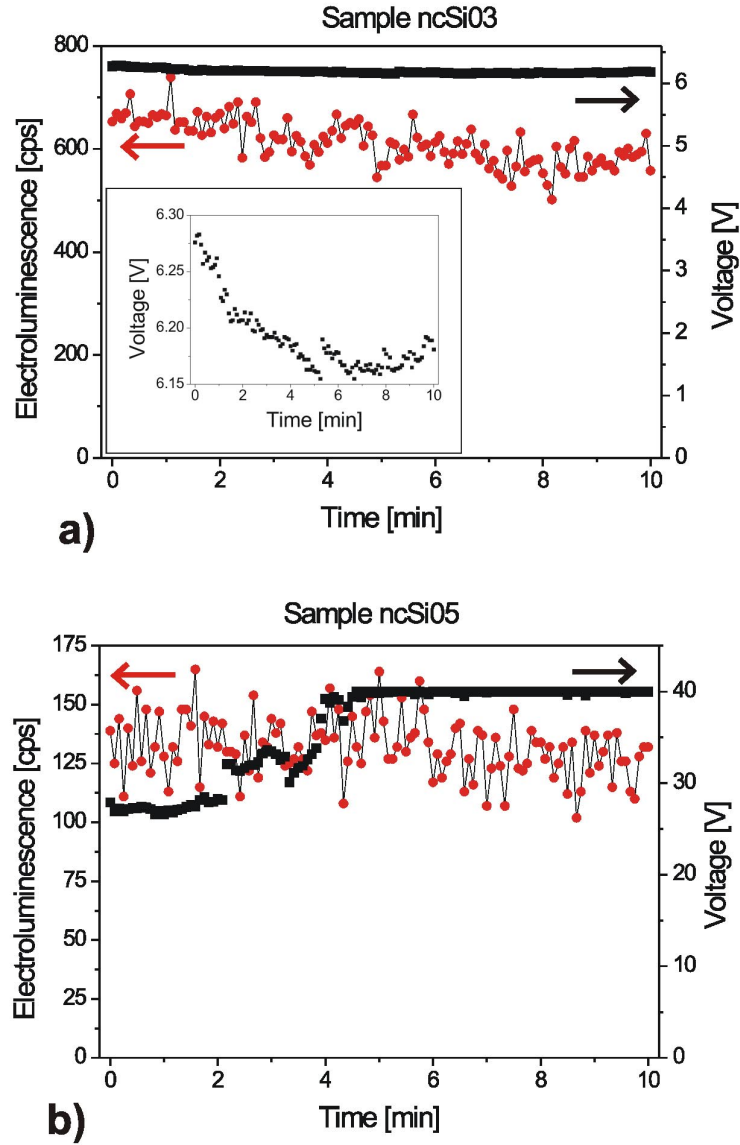


Figure 4.8: The time stability measurement of the sample ncSi03 (a) and ncSi05 (b). Constant current -10 mA (a) and 0.5 mA (b) was forced to flow through the samples and both the EL signal (red) and resulting voltage (black) were measured. The inset in (a) shows the voltage curve in more details. The compliance was set to 40 V.

4.2.4 Spectrally Integrated Electroluminescence with a Red Filter

As it was not possible to measure EL spectra, a filter was used to distinguish between the red region in which the emission of nc-Si is expected and the blue region of defect photoluminescence in SiO₂ (according to the photoluminescence spectra in Figure 4.2). A filter with the transmittance of about 60 % in the longer wavelength region and less than 5 % in the shorter wavelength region (with the edge at about 590 nm) was used (Figure 4.9).

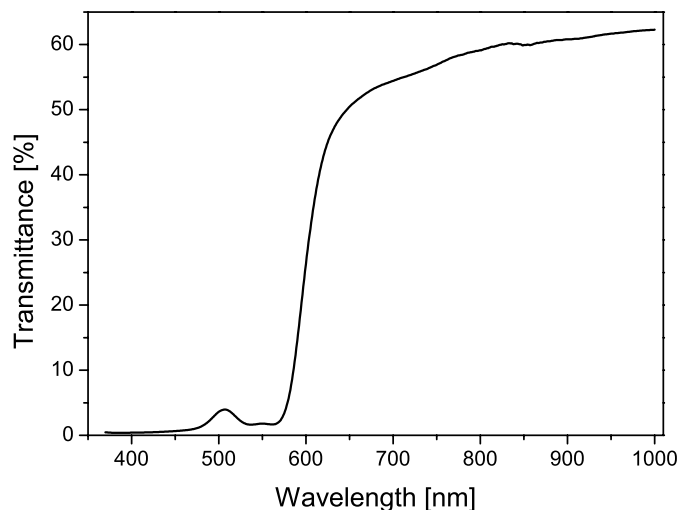


Figure 4.9: *The transmittance of the used filter as it was measured by a Shimadzu spectrometre.*

However, the measured spectra in Figures 4.10–4.12 show that the filter caused roughly the same decrease (to about a half of the original value) in all the measured samples. Therefore, the emission of all the samples must be situated, at least partially, in the same region in which the photoluminescence band of nc-Si is, i.e., above 590 nm.

The light emission from the reference sample ncSi02 can be attributed either to a silicon P-N junction reversely biased near the breakdown region [39], emitting light nearly over the whole visible range, or to the EL of neutral oxygen vacancies [40].

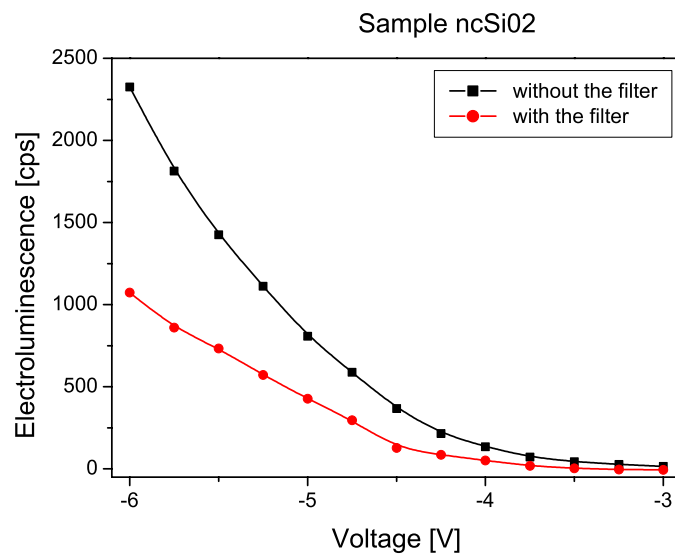


Figure 4.10: *The intensity of EL of the sample ncSi02 when measuring with and without the filter. The spectra are background-corrected.*

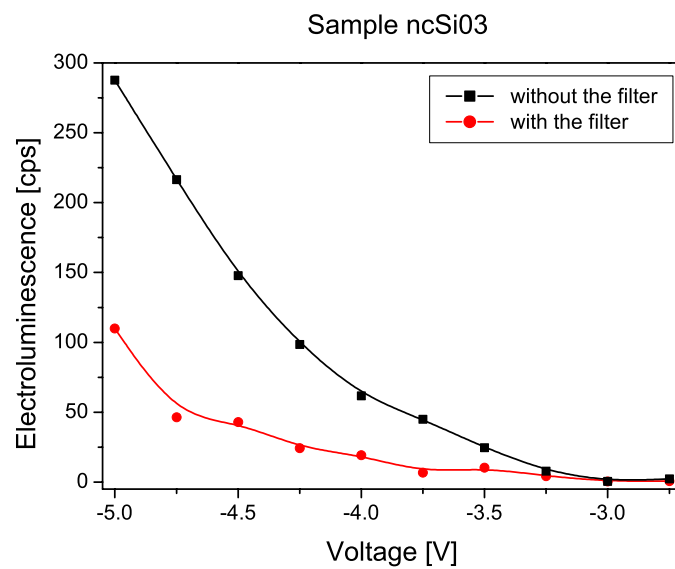


Figure 4.11: *The intensity of EL of the sample ncSi03 when measuring with and without the filter. The spectra are background-corrected.*

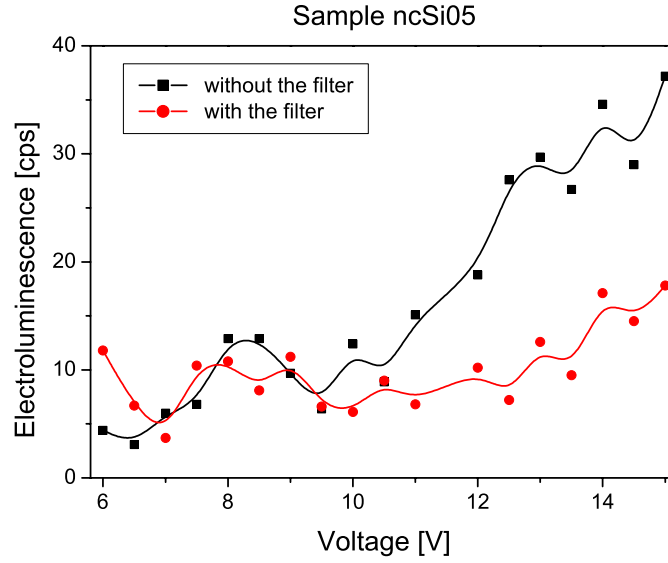


Figure 4.12: *The intensity of EL of the sample ncSi05 when measuring with and without the filter. The spectra are background-corrected.*

4.3 Transmission Measurements of the Ion Implanted Samples

The transmission measurements usually provides us with the transmission spectra of the samples which are important for the information on absorption. However, in our case, the transmission spectra were used for deriving the structure of our samples (namely, the position and the thickness of the nanocrystalline layer).

4.3.1 Results of the Transmission Measurements

The transmission of the ion implanted samples (Table 3.1) were measured by both a Fourier Transform Infrared (FTIR) spectrometre and a conventional spectrophotometre (*Shimadzu*). The measured spectra are shown in Figure 4.13.

The measurement with the spectrophotometre covers a wider range of wavelengths (250–2600 nm), especially the interesting region between 250 and 500 nm in which the nc-Si absorption edge is present. The onset of strong absorption (an abrupt decrease in transmission) shifts towards longer wavelengths with higher doses, or, in other words, towards lower photon energies with higher density of nanocrystals.

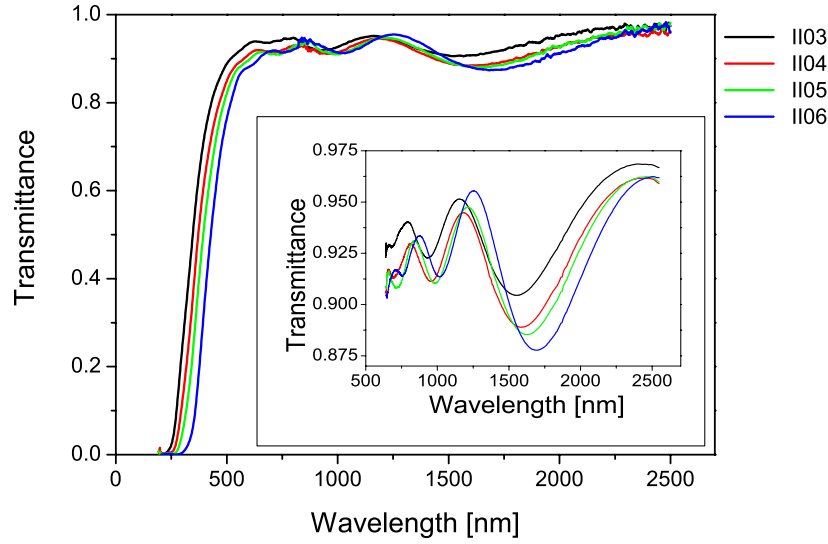


Figure 4.13: *The transmittance spectra of ion implanted samples measured by spectrophotometre and FTIR (in the inset).*

An interference pattern can also be seen at wavelength above the absorption edge. The problem is that the interference effects have significant influence in the absorption region, too, and may cause an error in deriving any absorption-related properties directly from these measurements [41]. Scattering losses should also be taken into account [42].

The FTIR transmission spectra will be helpful in understanding the interference patterns better. Even though they do not contain the region of the nc-Si absorption (the wavelength range is 600–2600 nm) their signal-to-noise is higher, and consequently they describe the interference patterns better. An important information that can be derived from the interference patterns is the actual composition of the samples (as the thickness of the implanted layer or the depth in which it is buried). More sophisticated models can even describe the profile of the refractive index throughout the layer. Moreover, by understanding the interference pattern and describing it quantitatively the extraction of absorption-related properties (such as Tauc gap) would become both possible and accurate.

The FTIR spectroscopy has many advantages, such as high spectral resolution without the need to use narrow slits and thus decrease the intensity or a quick measurement due to detecting the whole spectrum at once. However, there are some disadvantages, too, namely, the possible distortion of the measured spectrum. Therefore, the FTIR spectra were corrected by subtracting

a line background (with a very small slope) to match the spectrophotometre spectra as well as possible. Otherwise, the spectra measured by both above mentioned methods match in the overlapping region.

4.3.2 The Model of the Optical Properties of the Nanocrystalline Layer

In order to characterize the nanocrystalline layer, a model based on the Maxwell-Garnett formula (Equation (1.17)) for the permittivity of effective medium of a two-component material was introduced. The properties of nc-Si were approximated with the complex refractive index of crystalline silicon obtained from literature [43]; this material was embedded in the SiO_2 matrix with a constant real refractive index of 1.45 (setting the imaginary part κ to zero). Therefore, our model approximated the refractive index of the nanocrystalline layer by the Maxwell-Garnett effective complex refractive index. The refractive index can then be the function of fill factor f (Equation (1.18)) describing the nanocrystals-to-the-whole-layer volume ratio and thus characterizing the density of nc-Si in the layer. The curves resulting from our model are shown in Figure 4.14.

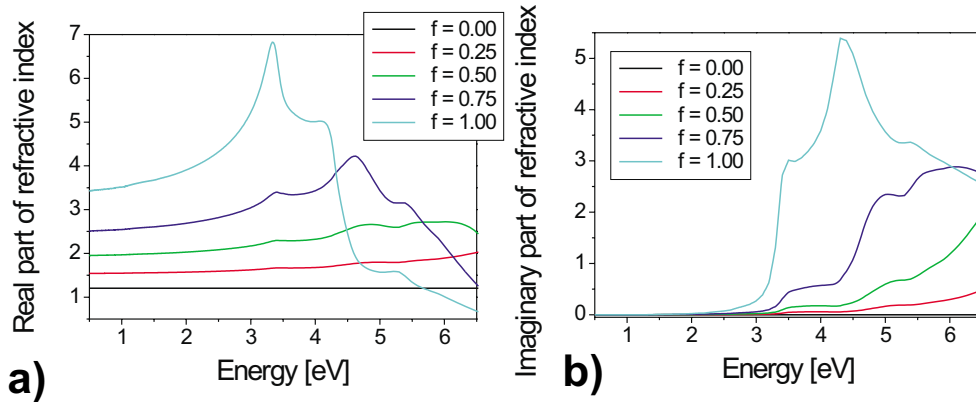


Figure 4.14: The real (a) and imaginary (b) parts of the complex refractive index of the $(\text{SiO}_2 + \text{nc-Si})$ layer estimated from the Maxwell-Garnett formula. The shape of the curve changes with fill factor f .

The fill factor influences the optical properties radically. The refractive index ranges from the refractive index of SiO_2 (if $f = 0$) to that of bulk silicon (if $f = 1$). The value of its real part strongly increases with increasing fill factor and the onset of the band is shifted towards lower energies. The onset of the band of the imaginary part is similarly shifted towards lower photon

energies with increasing fill factor, which qualitatively agrees with the same behaviour of the measured transmission spectra.

4.3.3 A Model of Interferences in a Thin Layer

The first simple model to explain the interference pattern in the transmission spectra was a Fabry-Perot interference in a single thin layer (1.27). The modelled sample consisted of a layer with the effective permittivity described above (standing for the nanocrystalline layer) which was thin enough (i.e., its thickness is less than the coherence length of the used light) to enable the interaction of the passing waves resulting into constructive and destructive interference. The SiO_2 substrate is considered too thick to allow the interference. Therefore no interference in the second medium is taken into account, the model spectra are only corrected for the reflection at the interface (though the influence of this correction is negligible). Normal incidence is assumed because the value of the angle of incidence in the measurement was 90° or very close to it.

In this model two parameters need to be adjusted: the fill factor f influencing the density of nanocrystals in the layer and thus the change in the (complex) refractive index, and the thickness t of the layer in which the interference occurs. The comparison of the measured spectra and the model transmission are depicted in Figure 4.15. The model obviously characterizes the main features of the measured spectra. The absorption region arising from the imaginary part of the crystalline-silicon refractive index roughly matches the absorption region of the measured data, however, the fit gets worse with increasing dose. The model absorption region can be shifted towards lower energy by increasing the fill factor when adjusting the parameters but the fill factor also affects the amplitude of the interferences. Thus the fill factor was set to match both these parameters without forcing it to describe the onset of absorption perfectly.

The separation between local maxima and minima in the model corresponds to those in the measured spectrum with the lowest dose perfectly. However, with increasing dose a variation in the separation is observed experimentally (Figure 4.15b, d, f, h), which does not appear in the model.

If both the thickness t and the fill factor f are known, it is possible to estimate the number of silicon ions in the layer simply from the volume essential to accommodate all the ions (supposing they make a typical lattice). Thus a simple formula of the “contents of silicon” can be derived as follows

$$C_{\text{Si}} = \frac{f \rho t}{A_r m_u} \quad (4.1)$$

from the atomic number of Si A_r , mass unit m_u and the density of crystalline

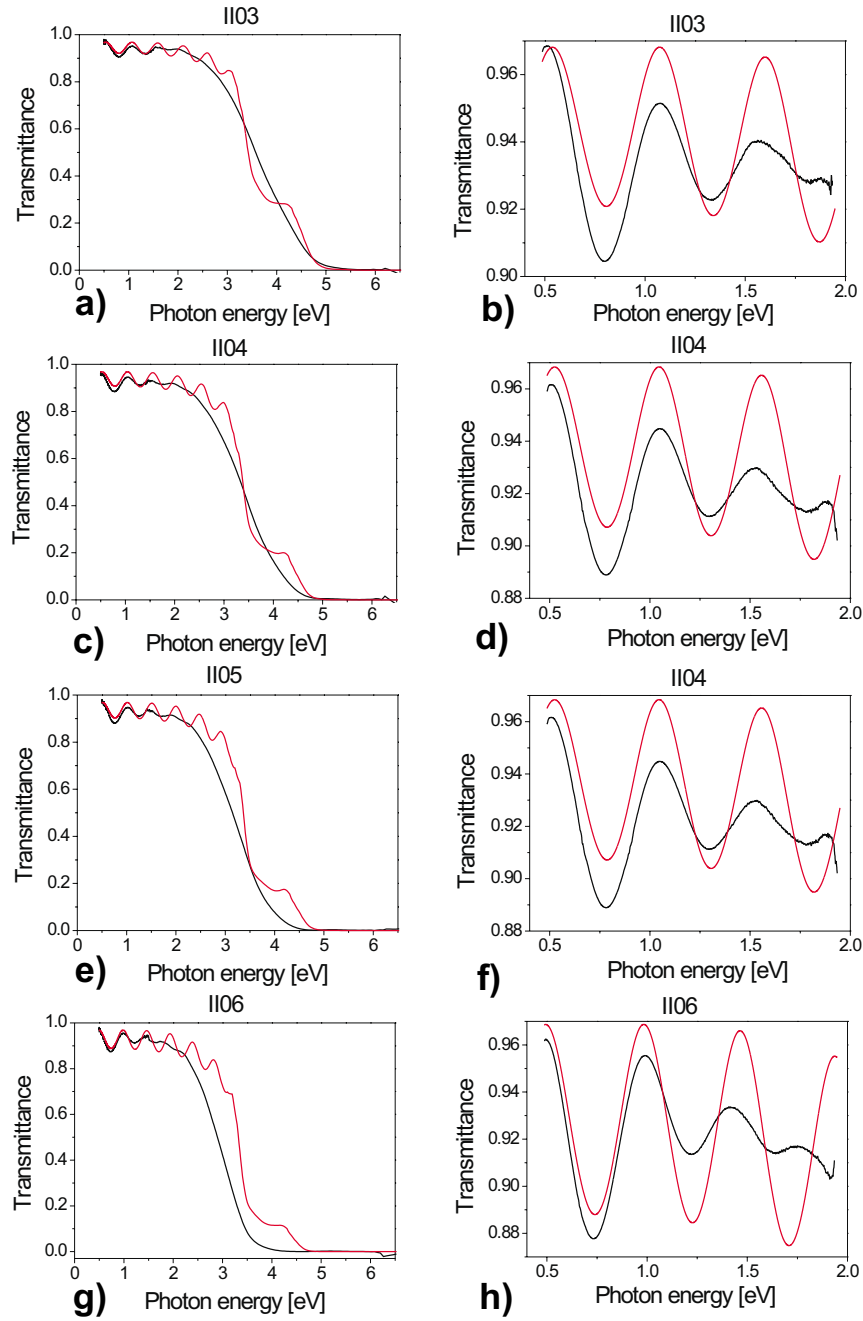


Figure 4.15: The comparison of the measured transmission spectra (black) and a simple model (red) of the interference in one thin layer. The data measured by FTIR (b, d, f, h) in the insets describes the interferences better than the data measured by a spectrometre (a, c, e, g).

silicon ρ . These estimated values of the silicon contents along with the parameters obtained by adjusting are summarized in Table 4.1. The estimated values of the contents of silicon correspond (taking into consideration the fact that the approximation of a single layer with constant refractive index is really rough) to the preparation parameters (dose) of individual samples even though the estimated values are slightly higher. The thickness of the layer is about 700 nm and slightly increases because of the shift of the positions of local maxima and minima in measured spectra.

Sample	Dose [10^{17}cm^{-2}]	t [nm]	f	C_{Si} [10^{17}cm^{-2}]	Difference
II03	3.0	715	0.12	4.3	43 %
II04	4.0	715	0.15	5.4	35 %
II05	5.0	730	0.16	5.8	16 %
II06	6.0	735	0.19	7.0	14 %

Table 4.1: *The values of parameters obtained by adjusting the one-layer-interference model to fit the measured spectra. The dose is compared to the value of the silicon contents estimated from adjusted parameters.*

Although some features mentioned above can be well described by this simple model, the model spectra completely lack the observed decrease in the amplitude of interferences. Therefore a second model was introduced.

4.3.4 A Model of Interference in Two Layers

The ions are not absorbed just under the surface of the glass during the implantation but they penetrates deeper. Consequently, there is a thin SiO_2 layer at the top part of the sample influencing the interferences. In order to take this fact into account a more complex model of the interference in two layers was considered.

The nanocrystalline layer was again characterized in the same way by the effective permittivity. The difference is in characterizing the interference patterns. In this case the interference in the system of two layers (the comparison with the previous model is displayed in Figure 4.16) was evaluated by means of the Abelés matrix method (see Section 1.10 for more details) assuming normal incidence again. The number of adjustable parameters therefore increased to three: the fill factor f , the thickness of the nanocrystalline layer t and the depth of the $\text{SiO}_2\text{-nc-Si}$ interface d .

The model spectra adjusted to best fit the measured ones are shown in Figure 4.17. The fit in the whole range of energies looks very similar to the one before. It is mainly because of the same requirement while adjusting

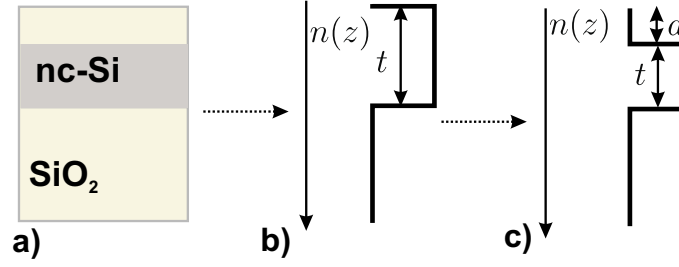


Figure 4.16: The sample (a) was described by a one-layer interference model (b) and then by a two-layer interference model (c).

on the correspondence of both the position of the absorption region and the amplitudes of the interference patterns. However, the second interference arising from the added layer modulates the pattern and thus it can change the amplitudes. This phenomenon can best be distinguished in the model interference pattern of the sample with highest dose (Figure 4.17h). The fact that in this case the positions of the peaks in the highest-dose spectrum match should also be noticed. The positions of the peaks change with varying thickness of the nanocrystalline layer while the depth remains constant.

The values of adjusted parameters in comparison with the estimated contents of silicon (Equation (4.1)) are depicted in Table 4.2. The increase in

Sample	Dose [10^{17}cm^{-2}]	d [nm]	t [nm]	f	C_{Si} [10^{17}cm^{-2}]	Difference
II03	3.0	120	620	0.12	3.7	23 %
II04	4.0	120	630	0.17	5.4	35 %
II05	5.0	120	630	0.19	6.0	20 %
II06	6.0	120	660	0.21	7.0	17 %

Table 4.2: The values of parameters obtained by adjusting the two-layer-interference model to fit the measured spectra. The dose is compared to the value of the contents of silicon estimated from the adjusted parameters.

the thickness of the nanocrystalline layer resembles the one estimated before and so does the correspondence between the theoretical value of the contents of silicon and the dose. The graphic representation along with the refractive index and the absorption coefficient as a function of energy evaluated from the fill factor and Maxwell-Garnett effective medium theory are displayed in Figure 4.18. Our model approximates the refractive index as a function of the depth in the sample only roughly but it takes into account absorption and dispersion.

In order to explain the decrease in the interference amplitude throughout the whole spectrum and thus describe the properties of the material better,

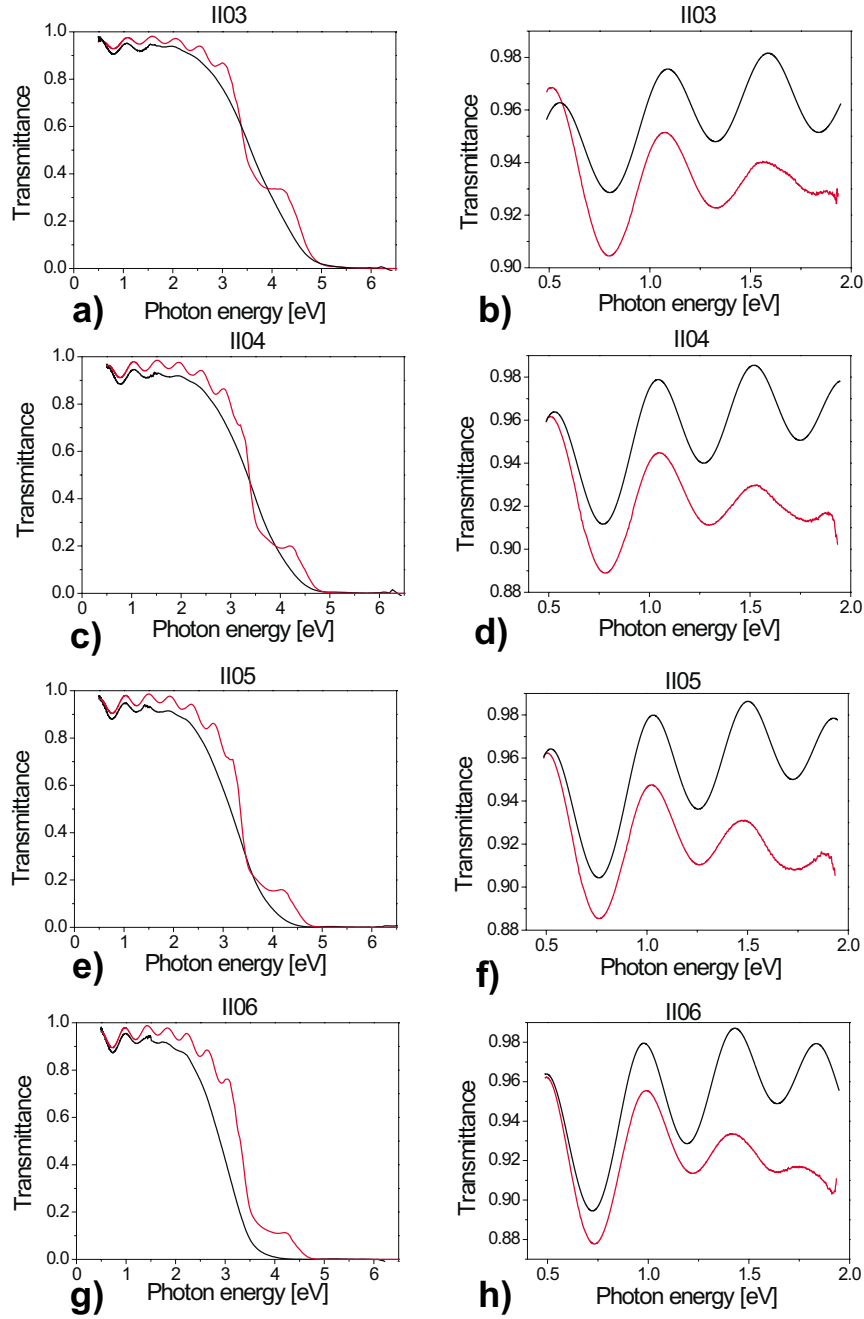


Figure 4.17: The comparison of the measured transmission spectra (black) and the model (red) of the interference in two thin layers. The data measured by FTIR (b, d, f, h) in the insets describes the interferences better than the data measured by a spectrometre (a, c, e, g).

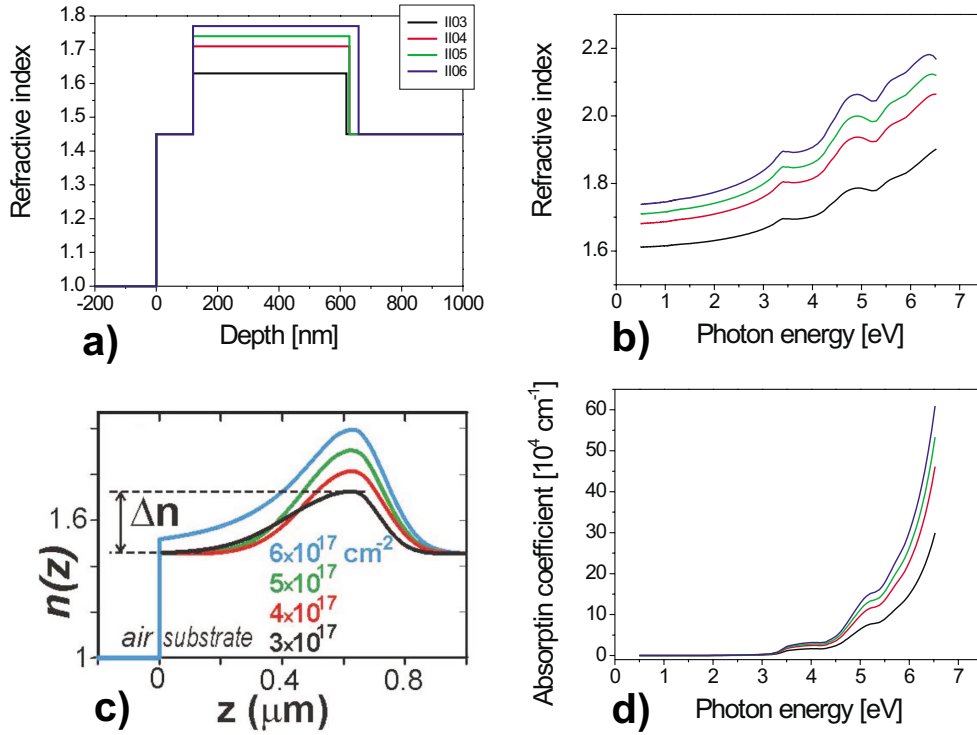


Figure 4.18: The model data for the refractive index and absorption coefficient derived from the adjusted fill factor. The refractive index as a function of the depth in the sample at 650 nm (a), compared to another refractive index model of the same samples (c) (after [21]), then the refractive index (b) and the absorption coefficient (d) as a function of energy can be seen.

an approach of continuously changing refractive index forming a peak (as in Figure 4.18c) instead of a step-like function (as in Figure 4.18a) must be taken [21].

Nevertheless, the main features of the measured spectra are characterized by this simple interference model in two layers. In Figure 4.18 the comparison between this profile of refractive index and a more sophisticated one made by T. Ostatnický [21] can be seen. In his model the profile of the refractive index is approximated with a Gaussian and a Lorentzian curve and the parameters of these curves are adjusted to best fit the interference patterns with the values for the refraction index of nanocrystalline silicon from literature used as starting point for the fit. No absorption or dispersion is taken into account. However, the step-like dependence and the peak agree with one another very well. The long tails of the peaks correspond to a very thin SiO_2 layer above the nanocrystals, in both cases the refractive index

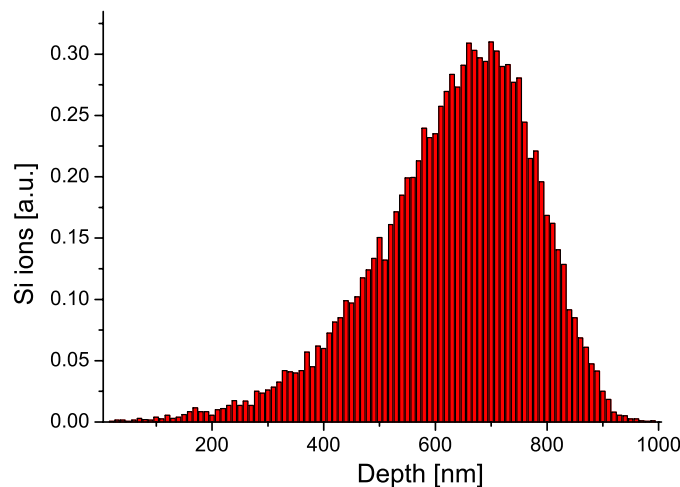


Figure 4.19: *The TRIM calculation of the Si^+ ions range in quartz.*

risers and the nanocrystalline layer gets a little thicker with increasing dose. The centres, widths and the differences between the values of the refractive indexes of the nc-Si layer and the substrate match, too.

There is one more point of view that can be useful when determining the refractive index of such a structure. The distribution of the implanted ions within the substrate can be modelled using a TRIM: SRIM-98 programme. This modelling was performed by J. Král, FJFI ČVUT, Prague. The result of modelling the implantation of 20,000 Si^+ ions with the energy of 400 keV into quartz (the dose cannot be taken into account) can be seen in Figure 4.19. Although the samples were annealed after the implantation the resulting profile of the nc-Si layer corresponds to the refractive index profile in Figure 4.18c.

Our results confirm not only the importance of interference effects in transmission spectra of implanted samples but also the use of the Maxwell-Garnett approximation as a beneficial tool for studying such materials.

4.4 Conductivity of the Ion Implanted Samples

In order to answer the question if the macroscopic lateral injection of carriers into the ion implanted samples is possible, the transport properties of such a system was measured. The adapted ion implanted sample II04P was used for this measurement and the experimental setup was the same as in EL

measurements (Figure 4.3). The acquired I - V curve is shown in Figure 4.20.

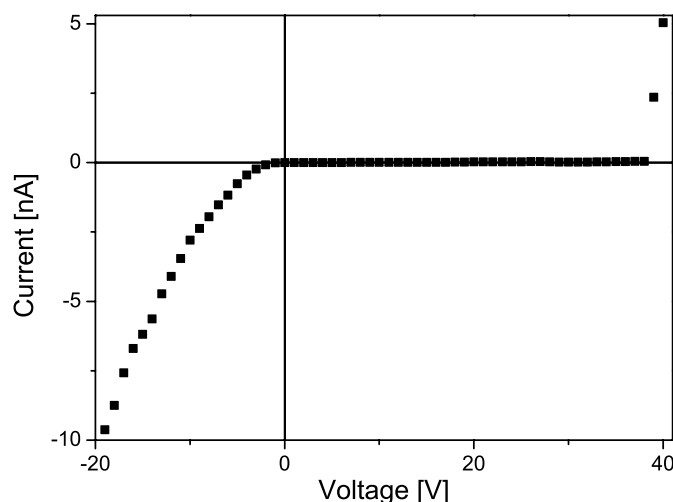


Figure 4.20: *The I - V curve of the ion implanted sample. The voltage was applied to the ITO contact.*

The conductivity of this structure can be evaluated to $4 \times 10^{-6} \Omega^{-1}\text{cm}^{-1}$. Obviously, the nanocrystals have created a conductive path in the glass allowing the tunnelling carriers to get through the layer. This is a positive message in view of the way towards an injection EL device. The I - V curve of the ion implanted sample is similar to that of a Zener diode.

The good electrical and optical properties of the ion implanted samples makes them a good candidate for PE-STM measurements.

4.5 Photon Emission Induced with an STM Tip

The STM-tip-induced photon emission (PE-STM) has emerged lately as a new way of studying light emitting materials with high spatial resolution. In this experiment, the STM tip is used as a source of low-energy electrons or holes of high brightness. The photons generated within the tunnelling process are then collected. Thus, extra information to the measured STM topography is obtained. This adds a “chemical contrast”—it is possible to distinguish between two materials which emit light with different efficiency.

Furthermore, not only the intensity of the photon emission, but also the spectra or the angular distribution of photons can be measured.

The use of the STM tip as a local optical probe allows us to study many physical phenomena, such as plasmons and interband transitions in metals, intrinsic luminescence and luminescent defects in semiconductors, molecular fluorescence, or photon emission from quantum-confined structures. We will focus on the photon emission from metals (since the films of silver or gold are used as a testing material in our case) and luminescence in semiconductors (as semiconductor nanostructures are to be studied by PE-STM in our group in the future).

4.6 The Theoretical Background of Scanning Tunnelling Microscopy

Scanning Tunnelling Microscopy (STM) is one of scanning probe techniques. It was discovered in 1981 by G. Binnig and H. R  hrer [44] who were soon (1986) awarded the Nobel Prize for their invention.

STM is a powerful means of imaging surfaces that can even reach the atomic resolution. It is based on the quantum mechanical phenomenon of tunnelling: if two conductive materials are brought close enough to each other and are biased, there is a non-zero probability of an electron getting through the barrier which isolates the surfaces. If we consider the simplest possible model of tunnelling between two metals, we will get the following relation for the tunnelling current I_t [45]:

$$I_t \sim V_t r_s \exp(-Kd\sqrt{\Phi}), \quad (4.2)$$

where V_t is the bias, r_s is the local density of states, K is a constant ($K \approx 10 \text{ nm}^{-1} \text{eV}^{-\frac{1}{2}}$), d is the tip-sample distance and Φ is the average barrier height. With two metals in vacuum, the barrier height is the average of their respective work functions.

The microscope can operate in various modes. The most important ones are the current-imaging and the constant-current modes:

A current-imaging mode: means that the tip position over the surface is kept unchanged and the topography is evaluated from the fluctuations in the current signal. This mode is not often used because the tip-sample distance is usually less than a nanometre but the typical sample roughness exceeds this value. The given conditions may cause a tip crush and consequently the tip is damaged. Therefore, this mode can only be operated with very flat surfaces.

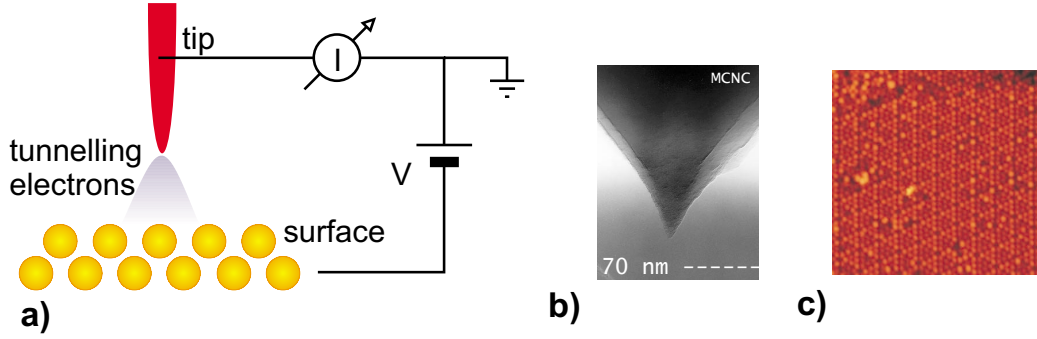


Figure 4.21: The basic scheme of STM operation (a), an etched tip (b), and the STM image with atomic resolution reconstruction (c), showing 7×7 reconstruction on Si(111) surface.

A constant current mode: is more convenient for most surfaces. When the tip scans the surface, the feedback loop controls the tunnelling current, keeping it constant by adjusting the bias. Thus, the tip follows the contours of the constant tip-sample distance d and the topography image $d(x, y)$ can be obtained without any risk of collision.

The most important advantage of this probe technique is its very high resolution. In the vertical direction the resolution can be less than a nanometre, depending on both the sharpness of the tip and the roughness of the studied surface. This can be achieved thanks to the strong distance dependence of the tunnelling current and the sensitivity of piezocrystals by which the tip is driven.

4.6.1 STM Measurements

The STM topographies of the samples prepared by spin-coating displayed in Figure 4.22 were measured using an ultra high vacuum (UHV) STM system in a constant current mode in Commissariat à l'Energie Atomique (CEA), Saclay, France. The tunnelling voltage was -2.0 V and the tunnelling current 500 pA.

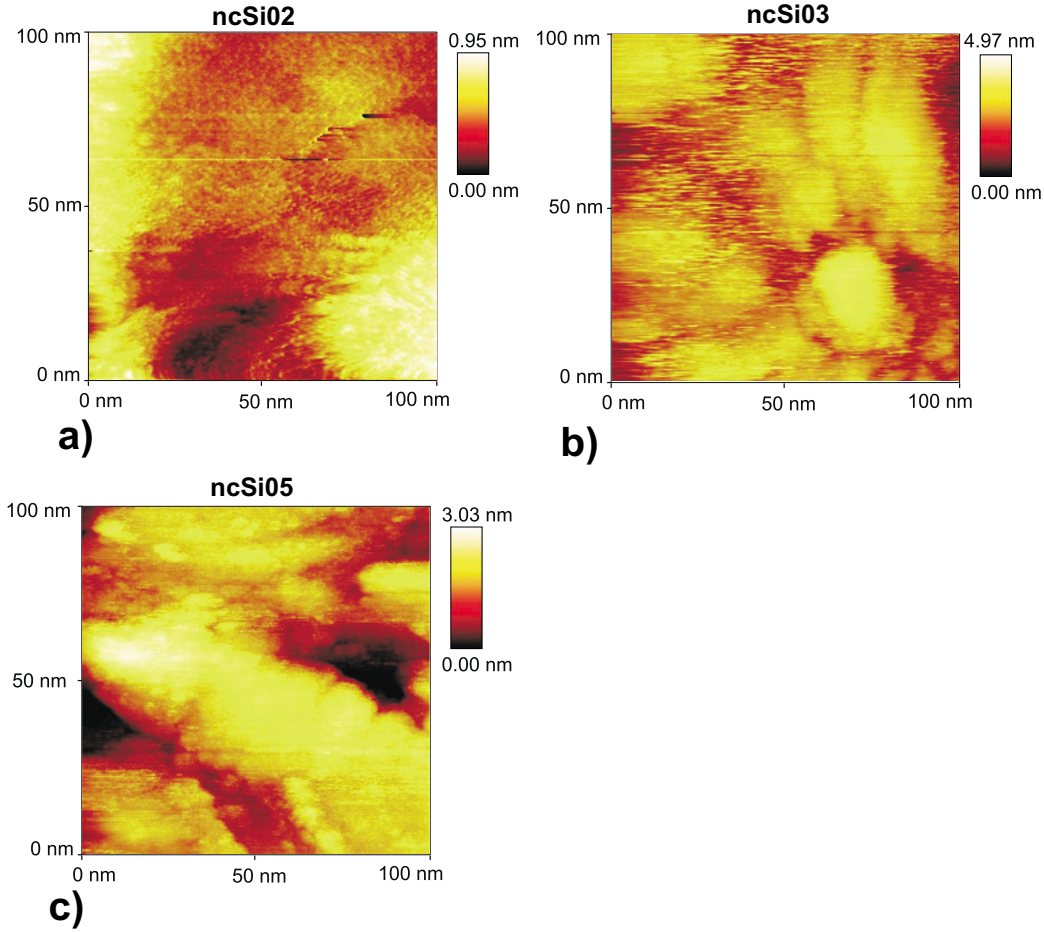


Figure 4.22: *STM topographies of the samples ncSi02 (a), ncSi03 (b), and ncSi05 (c).*

These images demonstrate that high spatial resolution can be achieved when using an STM system. The limitations of its use are, however, given by the requirement of sufficiently good transport properties to enable tunnelling.

If we compare individual topographies, we can see that the surface of the pure SiO_2 (ncSi02) is smoother (the range of the z -scale is only 1 nm) than the surfaces of the other two nanocrystalline samples (ncSi03 and ncSi05) with the z -scale reaching 5 nm and 3 nm, respectively. This difference is probably caused by the presence of nc-Si, or, more likely, nc-Si clusters. Thus, identifying the bumps on the surface as nanocrystalline clusters, the inhomogeneity of the distribution of single nanocrystals in the sample can be seen. Therefore, in order to improve the optoelectronic properties of these samples, the preparation method should be reviewed with special emphasis on the homogeneity of the resulting samples.

4.6.2 Photon Emission from Metals

One of the simplest models describing the STM-induced photon emission from metals [46] considers tunnelling from an s -like orbital at the apex of the tip to a spherical metallic particle. Thus, the probabilities of competing radiative and non-radiative processes can be estimated analytically. As the result, the inelastic-tunnelling-induced plasmon excitation shows as the most effective way of emitting a photon (with the probability in order of 10^{-3} photons per electron [46]).

The fact that the energy for the excitation of the plasmon comes from inelastic tunnelling, has one important consequence: both the materials of the tip and the sample and the geometry of the experiment influence emitted photons.

4.6.3 Photon Emission from Semiconductors

The STM-induced photon emission from semiconductors can arise due to various processes within the semiconductor sample. The kind of the process which occurs depends on both the energy of the tunnelling carriers and the type of a semiconductor. In the following processes electrons are assumed to be the tunnelling (injected) carriers. Similar mechanisms are possible with tunnelling holes, too.

- If the electron tunnels right into the minimum of a conduction band, the so-called **resonant tunnelling**, it can recombine radiatively.
- In case of higher energies, the tunnelling is followed by **hot electron decay** and again by the radiative recombination.
- If the energy of the tunnelling electron is higher of about the energy of the gap above the bottom of the conduction band, an electron in the sample can be excited from the valence band to the conduction one via the **Auger deexcitation** of the tunnelling electron. The excited electron then recombines radiatively.
- For very high tunnelling energies the **impact ionization** can occur.

In contrast to metals, in semiconductors the excitation energy originates largely from the excess energy of the elastically injected carrier. Therefore, the detected photon emission is influenced only by the sample, and the material of the tip (and the geometry of the setup) are not important.

4.6.4 Building the Experimental Setup for PE-STM

The usual value of the tunnelling current in an STM is about 1 nA, which corresponds to approximately 10^{10} tunnelling electrons per second. The value of the external quantum efficiency of the photon emission process can be 10^{-3} [46] at best. Furthermore, there will be additional losses in the detecting system arising from limited angle from which the light is collected (one or two orders of magnitude), and the limitation of the collecting/detecting chain (another one or two orders of magnitude). Then, the decrease in the acquired signal due to losses within transfer will be in order of 10^{-2} – 10^{-4} . However, the signal of about 10^3 – 10^5 cps can still be obtained (these values are summarized in Table 4.3). Because of low intensity of PE-STM, a sensitive detecting system is necessary.

current [electron/s]	10^{10}
the efficiency of photon emission	10^{-3}
losses in the collecting system	10^{-2} – 10^{-4}
resulting signal [photons/s]	10^3 – 10^5

Table 4.3: *The estimate of the signal acquired from PE-STM.*

The detecting system that we have built is displayed in Figure 4.23. In our case, the detecting system consists of two lenses and a detector. The first lens has the diameter of 45 mm and the focal length of 50 mm. It is aspheric to effectively collect the light emitted from a very small spot. The second lens is used to focus the collected light to the circular active area (with the diameter of $180\ \mu\text{m}$) of the detector; the lens' diameter is 8 mm and its focal length is 10 mm. As for the detector, a very sensitive commercial single photon counting module (*PerkinElmer SPCM-AQR*) is used. It was designed for the detection of low-intensity light (over the wavelength range of 400–1060 nm) and utilizes a silicon avalanche photodiode.

The used STM is a commercial microscope *Tescan* measuring in air shown in Figure 4.24. This microscope is used even though another STM measuring in UHV conditions and thus reaching higher resolution (*Omicron*) is available in FZÚ AVČR. However, both the manipulation with samples and the adjustment of the detecting system is much easier when utilizing the air-STM system. Therefore, the air-STM is more convenient for testing a detecting system that can later be adapted for the use in the UHV-STM.

The microscope is controlled by a special electronic unit operated with the software on a personal computer. This software was designed for measuring the STM topographies and local spectroscopy (I - V curves) but not for measuring the photon maps. In order to enable the measurement of a photon map, a photon counter was added to the avalanche photodiode and

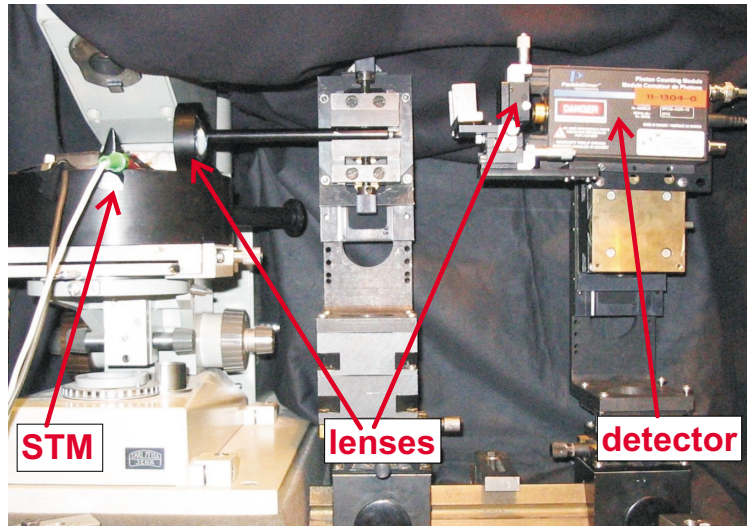
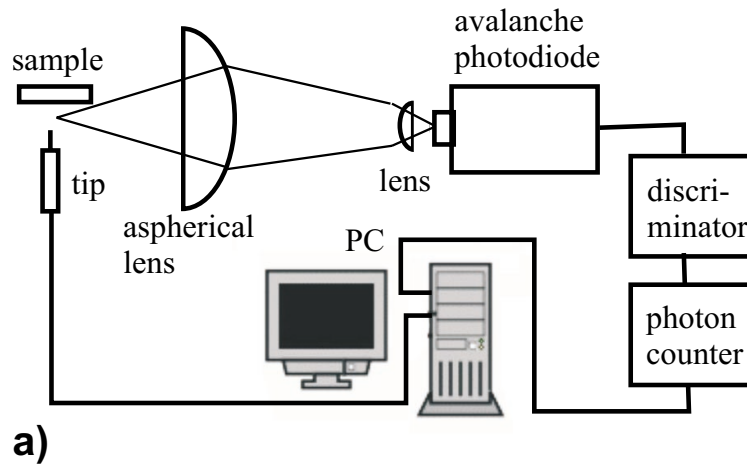


Figure 4.23: The scheme of the PE-STM setup (a) and the built setup with air-STM (b).

the whole system was connected with the computer via a GPIB interface. Afterwards, new software Surface Editing and Analysing (SEA) developed by M. Buček, FSI VUT, Brno was installed on the computer. The software is essential for displaying, modifying and saving the acquired photon maps.

The increase in the collected light intensity caused by the use of the second lens was measured using a LED with a shade and a pin-hole as a point source. The intensity was enhanced to 2400 cps with the second lens compared to 400 cps without it while the positions of the other parts of the collecting system remained unchanged. Thus, the second lens increases the intensity

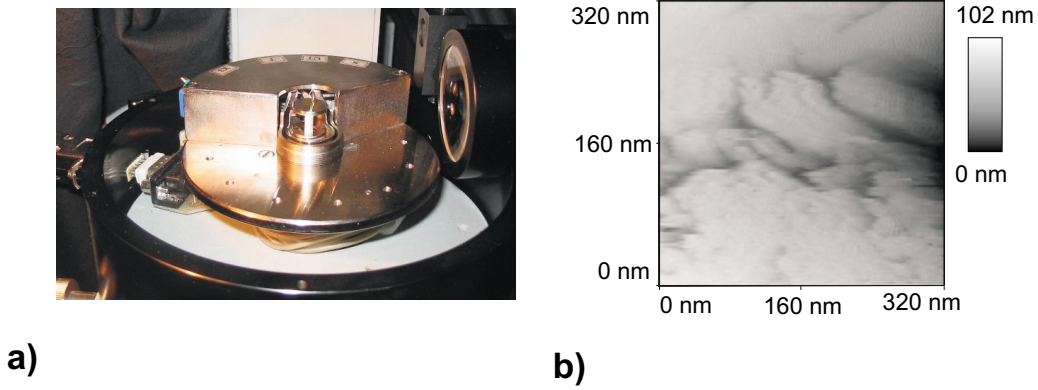


Figure 4.24: *The head of air STM microscope (a) and a topography of polycrystalline silver (b) measured by this microscope.*

of the collected light by the factor of about 6. The measured background of the whole setup is about 50 cps.

In order to adjust the detecting system as well as possible a modelling approach was undertaken. The simulation was performed by A. Svoboda, MFF UK, Prague using the OSLO software based on ray tracing. The distance between the tip-sample interface and the first lens d_1 was set to 50 mm. The distances between the first and the second lenses d_2 , and the second lens and a detector d_3 were optimized for obtaining the highest possible intensity of signal. The acquired parameters are depicted in Figure 4.25.

Another aim of the modelling approach was the quantitative description of the losses in the collecting system. As for the source, it was modelled as a Lambertian source, circular in shape with the radius of 1 μm emitting the light at the wavelength of 600 nm. 5×10^5 rays were launched and the previously obtained values of distances d_1 , d_2 , and d_3 (in Figure 4.25) were used. The image of the source made at the plane of the detector's active area was modelled by ray tracing and the results can be seen in Figure 4.26.

The resulting illuminated spot is quite small—it is a circle with the diameter between 100 and 200 μm , which means that the setup must be adjusted very sensitively. However, the irradiance as a function of the separation from the central point does not just simply decrease as the separation increases. On the contrary, it reaches values over 0.5 for the separation less than 50 μm , which makes the adjusting much easier compared to the situation when the irradiance steeply decreases as the separation from the central point increases.

The concrete shape of the irradiance curves is strongly dependent on the distance d_1 . The curves resulting from the same modelling differing only in the preset value of d_1 to 55 mm exhibited completely different behaviour containing only one maximum.

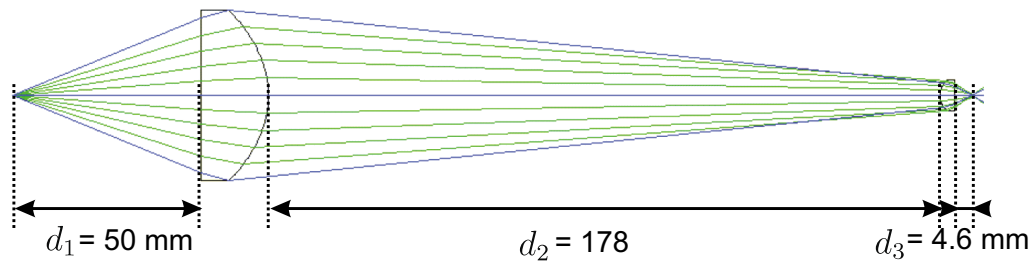


Figure 4.25: The optimized adjustment of the setup obtained by modelling.

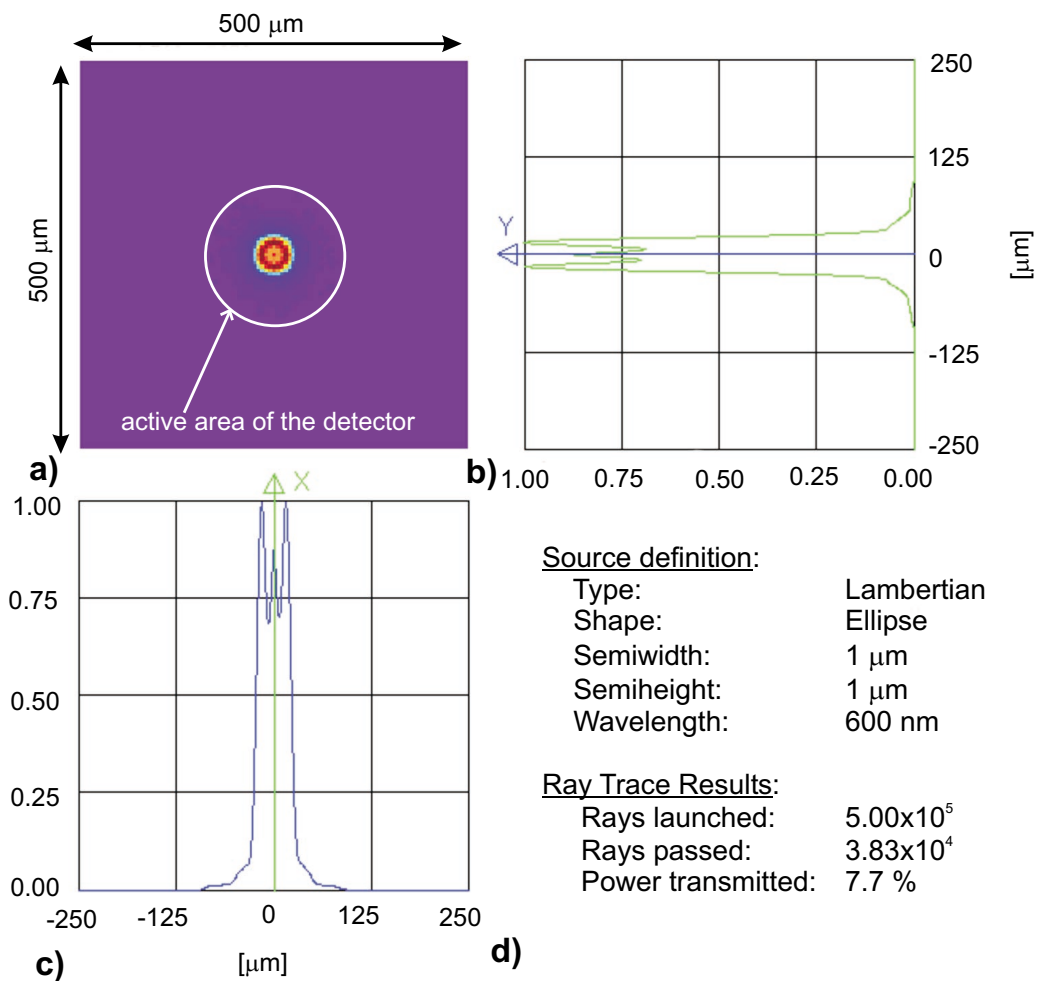


Figure 4.26: The modelled image of the source at the active area the the detector (a), its projections (b, c) and the description of modelling (d).

Concerning the efficiency of the detecting system, it will be characterized by the ratio of the power of the light incident on the active area of the detector to the power of the light emitted by the source (“transmitted power”). The value of the transmitted power was estimated to 7.7 %. Nevertheless, there is one important factor influencing the efficiency that was not included in the model, namely, the inclination of the source. In the model, the angle between the direction of maximum emission from the source and the axis of the collecting system is set to zero. In reality, the scanning with the STM takes place in the horizontal plane and the inclination angle was 90° . This inclination, obviously, causes additional losses that can be estimated at ten times less signal. Thus, the value of the transmitted power is in the order of several permilles, which agrees with the estimate made at the beginning of this subsection (summarized in Table 4.3).

As the result of the modelling, two ways to improve our detecting system can be found. Firstly, the whole collecting system can be inclined so that the angle between the maximum of the light emission and the axis of the collecting system could be less. However, if the angle between the maximum of the light emission and the axis of the collecting system was set to zero, the signal would be shaded by the tip. In this case, the ideal adjustment will probably be with the inclination of about 45° . Secondly, replacing the second lens by another aspherical one with larger diameter would increase the intensity, too.

Chapter 5

Discussion

The use of local luminescence probe that enables photon emission measurements with high spatial resolution, makes the study of light-emitting nanometre-sized objects possible. In a PE-STM measurement, local transport properties can be studied along with the optical ones. The aim of this master's thesis was to build an experimental setup for air-based PE-STM. This setup, unique in the Czech Republic, was started to be built with the future outlooks for studying the luminescence from silicon nanocrystals, a promising silicon-based light-emitting material. Therefore, emphasis was also put on studying optical and electronical properties of available nc-Si samples. The obtained results are summarized and discussed in the following sections.

5.1 Electrochemically Etched Silicon Nanocrystals

The first studied series of light-emitting silicon-based samples were nanocrystals prepared by electrochemical etching and subsequent spin-coating. The measured STM topographies (Figure 4.22) imply that the distribution of nc-Si in the SiO₂ layer is still quite inhomogeneous and the preparation method should be reviewed in order to obtain more homogeneous samples.

As for studying optoelectronic properties of these samples, the measured photoluminescence spectra (Figure 4.2) show the band centred at 720 nm of the light emission from nc-Si in the nanocrystalline samples and the absence of this band in the reference sample (pure SiO₂ on N-type Si). Furthermore, the samples exhibit reasonable electric conductivity across the (SiO₂+nc-Si)-layer ($\sim 10^{-7} \Omega^{-1}\text{cm}^{-1}$) and also a weak electroluminescence (Figures 4.4–4.6). An increase in the EL signal from the bias value of 4–5 V was observed under reverse polarity, indicating that impact ionization rather than bipolar

injection is the main excitation mechanism. The EL increase was followed by a decrease of both the current and the EL signal at the bias above 10–15 V caused probably by the dielectric breakdown in the SiO₂ layer. Consequently, the EL signal could not be increased by applying higher voltage to the samples.

The EL signal was too weak to enable the measurement of EL spectra but the luminescence is, at least partially, situated at the wavelength range above 600 nm, as can be seen from the EL measurements with a red filter (Figures 4.10–4.12).

The appearance of the EL signal from these samples could signify an important message, namely, achieving a conductive path through the nc-Si (a kind of percolation behaviour). What is, however, hard to understand in this context, is that the EL signal was obtained also from the reference sample free of nanocrystals. As this light emission is situated also above the wavelength of 600 nm, the light emission from the reference sample is probably caused by a P-N junction (or a Schottky barrier) biased in reverse direction [39] near the breakdown region or by neutral oxygen vacancies in pure but defect SiO₂ [40].

Therefore, no final conclusion concerning the mechanisms of EL from the nanocrystalline samples can be drawn yet. The possibility of different excitation mechanisms of photoluminescence and electroluminescence arises. The use of a sensitive CCD camera would probably enable the measurement of EL spectra revealing more details on the excitation mechanisms. Samples with higher degree of homogeneity of nc-Si distribution in SiO₂ layer are also needed.

5.2 Ion Implanted Silicon Nanocrystals

Another series of nc-Si samples was prepared by ion implantation, providing samples of high optical quality. The surprising results confirming an electrical transport (displayed in Fig 4.20) taking place between the individual nanocrystals in the matrix give rise to the possibility of using these samples for PE-STM measurements. The conductivity of the (SiO₂+nc-Si)-layer estimated from these measurements is in order of $10^{-6} \Omega^{-1}\text{cm}^{-1}$, which is a very high value compared to the conductivity of pure glass.

However, the STM tip must be placed directly above the nanocrystalline layer if the photon emission from nc-Si is to be measured successfully. Therefore, the ion implanted samples must be adapted similarly as they were for the conductivity measurement (the adaptation is shown in Figure 3.2) and the information on the position of the (SiO₂+nc-Si)-layer within the substrate is essential.

Therefore, the structure of the samples was obtained from a created interference model describing transmission spectra (Section 4.3). The model was based on the approximation of the (complex) refractive index of the ($\text{SiO}_2 + \text{nc-Si}$)-layer by the Maxwell-Garnett formula (Equation (1.17)). The dispersion and the absorption of the silicon material were also comprised in the model. The refractive index profile was then adjusted to fit the measured transmission spectra (Figure 4.17), acquiring the information on the position of the ($\text{SiO}_2 + \text{nc-Si}$)-layer within the substrate (about 500 nm thick layer reaching about 100 nm under the surface). In this model, two important facts were neglected: firstly, the refractive index as a function of the depth in the sample is definitely smoother than the assumed step-like function, and secondly, the size (and light emission) of nanocrystals in the layer was not taken into account. The nanocrystals were approximated with crystalline-silicon grains with size less than the wavelength of the used light instead. Nevertheless, the acquired parameters corresponded very well to other estimates (Figures 4.18c, 4.19) and the main features of the measured spectra, including the decrease in transmission attributed to the absorption of nc-Si, were characterized very well.

5.3 The Experimental Setup for PE-STM

In order to enable the measurement of spatially resolved photon emission with high resolution an experimental setup for PE-STM measurements has been built by adding a photon collecting system to an air-STM as is displayed in Figure 4.23. Both the adjustment and the efficiency of the collecting system were modelled. The resulting efficiency is sufficient to obtain photon emission from samples of polycrystalline silver or gold in which the efficiency of the radiative decay of plasmon is high (10^{-3}). Even though the modelled parameters and the testing materials of polycrystalline silver and gold were used, no photon emission excited by tunnelling carriers injected into the samples was observed so far. The answer to the question why is very difficult and more studies need to be performed.

Therefore, the question why no photon emission was observed remains, for the time being, unanswered. However, the work on this experiment will be continued by the author of this master's thesis during her future PhD. studies in the collaboration with the Nanophotonics group in Commissariat à l'Energie Atomique, Saclay, France.

Chapter 6

Conclusions

This master's thesis was focused on the study of silicon nanocrystals and also on the participation on building the experimental setup for measuring photon emission induced with the tip of a scanning tunnelling microscope. This system will allow to study the optoelectronic properties of nanometre-sized light-emitting centres with high spatial resolution.

- A weak electroluminescence signal from the samples prepared by embedding electrochemically-etched silicon nanocrystals in an SiO_2 matrix by spin-coating was observed. Nevertheless, the distribution of nanocrystals in the SiO_2 layer is still inhomogeneous and more homogeneous samples are needed.
- An interference model of the transmission spectra of samples of ion implanted silicon nanocrystals was created. The information on the structure of these samples was obtained by comparing the model spectra with the measured ones. Furthermore, the existence of the electrical transport between individual silicon nanocrystals in the silica glass was confirmed. Both the electrical properties and the structure of the samples are crucial for possible future PE-STM measurements.
- The experimental setup for measuring air-based PE-STM was built and tested. In order to adjust the setup as well as possible the ideal adjustment was modelled. Besides, some suggestions for improving the performance of the setup were obtained from the modelling. However, the proper adjustment of the setup requires further effort.

Bibliography

- [1] L. Pavesi, in *Photonics Packaging and Integration III*, Vol. 4997 of *Proceedings of SPIE*, edited by R. A. Heyler, D. J. Robbins, and G. E. Jabbour (Photonic West, San Diego, 2003), Chap. A review of the various efforts to a silicon laser, pp. 206–220.
- [2] S. A. Chambers, *Materials Today* **5**, 34 (2002).
- [3] E. Suhir, *The Future of Microelectronics and Photonics, and the Role of Mechanical, Materials and Reliability Engineering*, outline of a key-note talk, MicroMat 2000, Berlin, 2000.
- [4] D. J. Lockwood, in *Light Emission in Silicon: From Physics to Devices*, Vol. 49 of *Semiconductors and Semimetals*, edited by D. J. Lockwood (National Research Council, Institute for Microstructural Sciences, Ottawa, Canada, 1998), Chap. Light Emission in Silicon, pp. 11–13.
- [5] S. S. Iyer and Y.-H. Xie, *Science* **260**, 40 (1993).
- [6] A. Gustafsson, M.-E. Pistol, L. Montelius, and L. Samuelson, *Journal of Applied Physics* **84**, 1715 (1998).
- [7] E. B. Shera, N. K. Seitzinger, L. M. Davis, R. A. Keller, and S. A. Soper, *Chemical Physics Letters* **174**, 553 (1990).
- [8] J. Lindahl, M.-E. Pistol, L. Montelius, and L. Samuelson, *Applied Physics Letter* **68**, 60 (1996).
- [9] K. Yamanaka, K. Suzuki, S. Ishida, and Y. Arakawa, *Applied Physics Letter* **73**, 1460 (1998).
- [10] A. Gustafsson, M.-E. Pistol, M. Gerling, L. Samuelson, M. R. Leys, and H. Titze, *Journal of Applied Physics* **70**, 1660 (1991).
- [11] D. L. Abraham, A. Veider, C. Schönenberger, H. P. Meier, D. J. Arent, and S. F. Alvarado, *Applied Physics Letters* **56**, 1564 (1990).

- [12] Y. Khang, Y. Park, M. Salmeron, and E. Weber, Review of Scientific Instruments **70**, 4595 (1999).
- [13] J. Valenta, R. Juhasz, and J. Linnros, Journal of Luminescence **98**, 15 (2002).
- [14] A. Gustaffson and L. Samuelson, Physical Review B **50**, 386 (1992).
- [15] E. S. Kwaak and D. A. V. Bout, Analytica Chimica Acta **496**, 259 (2003).
- [16] R. Berndt, in *Scanning Probe Microscopy—Analytical Methods*, edited by R. Wiesendanger (Springer-Verlag, Berlin, Heidelberg, 1998).
- [17] S. F. Alvarado, P. Renaud, D. L. Abraham, C. Schönenberger, D. J. Arent, and H. P. Meier, Journal of Vacuum Science and Technology B **9**, 409 (1991).
- [18] P. Fojtík, Ph.D. thesis, MFF UK, 2003.
- [19] L. Pavesi, L. D. Negro, C. Mazzoleni, G. Franzo, and F. Priolo, Nature Materials **408**, 440 (2002).
- [20] K. Ito, S. Ohyama, Y. Uehara, and S. Ushioda, Surface Science **363**, 423 (1996).
- [21] J. Valenta, T. Ostatnický, I. Pelant, P. Janda, R. G. Elliman, J. Linnros, and . B. Hönerlage, submitted to *Physical Review Letters*, 2004.
- [22] M. H. Pilkuhn and W. Schairer, in *Device Physics*, Vol. 4 of *Handbook On Semiconductors*, edited by C. Hilsum (North-Holland, Amsterdam, the Netherlands, 1993), Chap. Light Emitting Diodes, pp. 614–631.
- [23] J. Maxwell-Garnett, Philosophical Transactions of the Royal Society **203**, 385 (1904).
- [24] F. Abelés, Annals of Physics **5**, (1950).
- [25] J. Křepelka, *Optika tenkých vrstev* (Univerzita Palackého, Olomouc, 1993), Vol. 58.
- [26] J. Brož, V. Roskovec, and M. Valouch, *Fyzikální a matematické tabulky* (SNTL — Nakladatelství technické literatury, Praha, 1980).
- [27] <http://hyperphysics.phy-astr.gsu.edu/hbase/tables/elabund.html>, the web page of Thomas Jefferson National Accelerator Facility – Office of Science Education.

- [28] D. G. Thomas, M. Gershenzon, and J. J. Hopfield, *Physical Review* **131**, 2397 (1963).
- [29] M. E. Castagne, S. Coffa, M. Monaco, L. Caristia, A. Messina, R. Mangano, and C. Bongiorno, *Physica E* **16**, 547 (2003).
- [30] A. Polman, *Nature Materials* **1**, 10 (2002).
- [31] L. T. Canham, *Applied Physics Letters* **57**, 1064 (1990).
- [32] L. D. Negro, M. Cazzanelli, N. Daldosso, Z. Gaburro, L. Pavesi, F. Priolob, D. Pacifici, G. Franzo, and F. Iacona, *Physica E* **16**, 297 (2003).
- [33] I. Umezu, G. Yamazaki, T. Yamaguchi, A. Sugimura, T. Makino, Y. Yamada, N. Suzuki, and T. Yoshida, *Materials Science and Engineering: C* **15**, 129 (2001).
- [34] Q. Zhang, S. C. Bayliss, and D. A. Hutt, *Applied Physics Letters* **66**, 1977 (1995).
- [35] S. Aihara, R. Ishii, M. Fukuhara, N. Kamata, D. Terunuma, Y. Hirano, N. Saito, M. Aramata, and S. Kashimura, *Journal of Non-Crystalline Solids* **296**, 135 (2001).
- [36] P. D. Townsend, P. J. Chandler, and L. Zhang, in *Optical Effects of Ion Implantation*, Vol. 13 of *Cambridge Studies in Modern Optics*, edited by P. L. Knight and A. Miller (Cambridge University Press, Cambridge, Great Britain, 1994).
- [37] V. Švrček, I. Pelant, J. L. Rehspringer, P. Gilliot, D. Ohlmann, O. Crégut, B. Hönerlage, T. Chvojka, J. Valenta, and J. Dian, *Materials Science and Engineering C* **19**, 233 (2002).
- [38] K. Dohnalová, Master's thesis, MFF UK, 2003.
- [39] R. Newman, *Physical Review* **100**, 700 (1955).
- [40] H. S. Bae, T. G. Kim, C. N. Whang, S. Im, J. S. Yun, and J. H. Song, *Journal of Applied Physics* **91**, 4078 (2002).
- [41] R. G. Elliman, M. J. Lederer, and B. Luther-Davies, *Applied Physics Letters* **80**, 1325 (2002).
- [42] A. Dowd, R. G. Elliman, and B. Luther-Davies, *Applied Physics Letters* **79**, 2327 (2001).

- [43] D. F. Edwards, in *Handbook of Optical Constants of Solids*, edited by E. D. Palik (Academic Press, inc., New York, 1985), Chap. Silicon, pp. 547–569.
- [44] G. Binning and H. Rohrer, *Ultramicroscopy* **11**, 157 (1983).
- [45] B. A. Sexton, in *Surface Analysis Methods in Materials Science*, Vol. 29 of *Springer Series in Surface Sciences*, edited by D. J. O'Connor, B. A. Sexton, and R. S. C. Smart (Springer Verlag, Berlin, 1992), Chap. Scanning Tunneling Microscopy, pp. 221–244.
- [46] B. N. J. Persson and A. Baratoff, *Physical Review Letters* **67**, 3224 (1992).

CURRICULUM VITAE

Personal Data

- Name and surname: **Kateřina Kůsová**
- Date of birth: 15 July 1981
- Nationality: Czech

Education

- Higher Education: 1999 - (2004)
studying for Master Degree
Faculty of Mathematics and Physics
Charles University, Prague, the Czech Republic
- Specialization: **Optics and Optoelectronics** (since 2002)

Other Activities Related to Education

- two **students projects** (2000 - 2001, 2001 - 2002) focused on
 - the temperature dependence of photoluminescence spectra of CdS and CdSe nanocrystalline thin layers
 - photoluminescence decay of CdS and CdSe nanocrystals embedded in glass matrices
- a **research stay** (June–July 2003) at University of Barcelona

Publications

- Study of Optoelectronic Properties of Light-Emitting Silicon-Based Materials with High Spatial Resolution - a **poster** at the 3rd aSiNet workshop, Bratislava, 2004

Other Skills

- advanced knowledge of English
- basic passive knowledge of French
- basic computer skills (MS Windows, Office, basics of Delphi, ...)